The Astronomical Journal, 165:154 (21pp), 2023 April https://doi.org/10.3847/1538-3881/aca971

Spectroscopic Study of Ba and CEMP-*s* Stars: Mass Distribution of AGB Progenitors*†

Partha Pratim Goswami[1,2] and Aruna Goswami[1]
[1] Indian Institute of Astrophysics, Koramangala, Bangalore 560034, India; partha.pg@iiap.res.in, ppg0024@gmail.com
[2] Pondicherry University, R.V. Nagar, Kalapet, 605014 Puducherry, India
Received 2022 May 5; revised 2022 November 29; accepted 2022 November 30; published 2023 March 10

Abstract

We have performed detailed high-resolution spectroscopic analysis on seven metal-poor stars (BD+75 348, BD +09 3019, HD238020, HE0319–0215, HE0507–1653, HE0930–0018, HE1023–1504) and derived their atmospheric parameters $T_{\rm eff}$, log g, [Fe/H], and microturbulent velocity (ξ). The metallicity range is found to be $-2.57 < [{\rm Fe/H}] < -0.42$. The elemental abundances of 17 light elements and 12 heavy elements are estimated. We have classified BD+75 348 and BD+09 3019 as strong Ba stars, HD238020 as a mild Ba star, and the remaining four objects as CEMP-*s* stars. We have estimated the masses of the stars from Hertzsprung–Russel (HR) diagram, and, compiling the data of 205 Ba stars from literature, estimated the mass distribution of Ba stars. We have also estimated the initial masses of the companion AGBs of the program stars as well as the masses of the companion AGBs of 159 Ba and 36 CEMP-*s* stars from literature, with the help of a parametric-model-based analysis using FRUITY models. While the primary mass distribution of mild Ba stars peaks at 3.7 $M_{\odot}$, for the strong Ba stars the peak appears at 2.5 $M_{\odot}$. We, therefore, propose that the initial masses of the progenitor AGBs dominantly control the formation of mild and strong Ba stars. However, a clear overlap, in the range 1.3–4.0 $M_{\odot}$, noticed between the progenitor masses of both the subclasses of Ba stars, may indicate that other factors, such as the metallicities and the orbital periods, may also have significant contributions. The progenitor AGBs' mass distribution of CEMP-*s* stars is found to peak at 2.03 $M_{\odot}$.

Unified Astronomy Thesaurus concepts: CEMP stars (2105); Barium stars (135); Carbon stars (199); Chemically peculiar stars (226); Hertzsprung Russell diagram (725); Stellar physics (1621); Asymptotic giant branch stars (2100); Chemical abundances (224); S-process (1419); Spectroscopy (1558)

Supporting material: machine-readable tables

1. Introduction

Barium (Ba) stars and a subclass of carbon-enhanced metal-poor (CEMP) stars, known as CEMP-*s* stars, exhibit enhanced abundances of elements produced by slow (s-) neutron (n)-capture process. Ba stars, first recognized by Bidelman & Keenan (1951), are identified by the presence of strong absorption lines of Ba II at 4554 Å and Sr II at 4077 Å in their spectra (Warner 1965). C_2, CN, and CH molecular bands are also prominent in Ba stars. Depending on the types of neutron-capture elements present, CEMP stars are divided into four subclasses (Beers & Christlieb 2005; Frebel 2018; Goswami et al. 2021), namely, CEMP-*s* stars (enriched with *s*-process elements), CEMP-*r* stars (enriched with elements produced in rapid n-capture process or r-process), CEMP-*r*/*s* stars (enriched with elements produced by the intermediate n-capture process or *i*-process; Cowan & Rose 1977; Herwig et al. 2011; Doherty et al. 2015; Hampel et al. 2016; Banerjee et al. 2018; Denissenkov et al. 2019; Goswami et al. 2021), and CEMP-no stars (not enriched with n-capture elements).

The formation scenario of CEMP-*s* (Spite et al. 2013) and Ba (Cseh et al. 2018, 2022) stars is similar. Both types of stars (secondary) are extrinsic in nature, and they obtain *s*-process-rich material through mass transfer from a more massive companion (primary), which evolves faster and produces *s*-process elements in the AGB phase. CEMP-*s* and Ba stars are known to be in binary systems with invisible white-dwarf companions. The binary nature of these stars is proved by long-term radial velocity monitoring programs (McClure 1983, 1984; McClure & Woodsworth 1990; Lucatello et al. 2005; Starkenburg et al. 2014; Hansen et al. 2016; Jorissen et al. 2016). Recent studies (Hampel et al. 2016; Roederer et al. 2016; Hampel et al. 2019; Koch et al. 2019; Goswami & Goswami 2020; Goswami et al. 2021) have revealed that one of the formation scenarios for CEMP-*r*/*s* stars might also be the binary evolution with contamination by AGB yields similar to that of CEMP-*s* stars. The different physical conditions between the production of *s*- and *i*-process elements in AGB stars are still under debate. In our recent study (Goswami & Goswami 2022), we have reported object HE 1005–1439, the abundance pattern of which shows contamination by both *s*- and *i*-processes. We proposed that, in AGB stars, *s*- and *i*-process can take place in succession without masking the signatures of each other. Although the formation scenarios of Ba, CEMP-*s*, and CEMP-*r*/*s* stars are similar, in this paper, we will discuss only CEMP-*s* and Ba stars. Warner (1965) classified Ba stars using Ba indexes of 1–5 based on the strength of the Ba II 4554 Å line. Ba1 and Ba5 signify stars showing the weakest and the strongest Ba lines, respectively. Later, several authors (Lu 1991; Jorissen et al. 1998; Yang et al. 2016; Escorza et al. 2017) used this Ba index to classify the Ba stars into two groups: mild Ba stars and strong Ba stars. The overabundance of n-capture elements is higher in strong

* Based [in part] on data collected at Subaru Telescope, which is operated by the National Astronomical Observatory of Japan.
† [Part of] the data are retrieved from the JVO portal (http://jvo.nao.ac.jp/portal) operated by the NAOJ.

Ba stars than in mild Ba stars. In the literature, lower enhancement of heavy elements in mild Ba stars is explained by two plausible formation scenarios: (i) a longer orbital period of the binary system, and (ii) relatively weaker neutron exposure in the AGB companion that pollutes the star (Yang et al. 2016).

In this paper, we have reported the elemental abundances of seven stars, BD+75 348, BD+09 3019, HD 238020, HE 0319–0215, HE 0507–1653, HE 0930–0018, and HE 1023–1504, based on detailed high-resolution spectroscopic analysis. We have estimated the masses of the program stars and their AGB companions. We have estimated the masses of several Ba stars found in the literature to find the mass distribution of these stars. We have also derived the initial mass distribution of the AGB companions of these Ba stars and a sample of literature CEMP-*s* stars. Here, we refer to the stars (Ba and CEMP-*s*) that we are observing now as secondary stars and to their companion AGBs as primary stars.

We have organized the paper as follows. In Section 2 we summarize the earlier studies available in the literature on our program stars. The details of the sources of the spectra are presented in Section 3. In Section 4, we discuss the method of determining the photometric temperatures. Section 5 discusses the method of estimating the radial velocity and deriving the stellar atmospheric parameters of the program stars. In Section 6 we present the abundance analysis results (Section 6.1) and the kinematic analysis of the program stars (Section 6.2). In Section 7 we present (i) the classification schemes of Ba and CEMP-*s* stars (Section 7.1), (ii) the classification of the program stars (Section 7.2), (iii) the determination of masses of the program stars (Section 7.3), (iv) the determination of masses of the primary companions (AGB progenitors) of the program stars (Section 7.4), (v) a comprehensive discussion on the mass distributions of a literature sample of Ba stars and their AGB progenitors and the mass distribution of the AGB progenitors of a literature sample of CEMP-*s* stars (Section 7.5), and (vi) the formation scenarios of mild and strong Ba stars (Section 7.6). Section 8 draws the conclusions.

2. Previous Studies of the Program Stars

2.1. BD+09 3019, HD 238020, HE 0930–0018, and HE 1023–1504

BD+09 3019 is included in the carbon star catalog of Stephenson (1989), CH star catalog of Bartkevicius (1996), and the carbon star catalog of Ji et al. (2016) from LAMOST 2 data. HD 238020 is included in the CH star catalog of Bartkevicius (1996). The list of faint high-latitude carbon stars of Christlieb et al. (2001) includes HE 0930–0018 and HE 1023–1504. The atmospheric parameters of BD+09 3019 and HE 0930–0018 are not reported previously in the literature. McDonald et al. (2012) derived the effective temperatures of HD 238020 using the spectral energy distribution (SED) method of temperature calibration. Our estimate of the temperature is greater by 115 K for HD 238020 than that of McDonald et al. (2012). Kennedy et al. (2011) estimated the atmospheric parameters and the abundance of oxygen for HE 1023–1504. Our estimates of the effective temperature and log *g* closely match the estimates of Kennedy et al. (2011). However, the metallicity ([Fe/H]) estimated by Kennedy et al. (2011) is ∼0.8 dex lower than that of our estimate. Figure 1 shows the spectrum synthesis fits of a few Fe I lines in the spectrum of HE 1023-1504 using the atmospheric parameters of our study. In this work, first-time abundance estimates of several light elements from C through Zn and neutron-capture elements from Sr through Hf are presented for these four objects based on high-resolution spectroscopic analysis.

2.2. BD+75 348, HE 0319–0215, and HE 0507–1653

BD+75 348 is listed in the carbon star catalog of Stephenson (1989) and CH star catalog of Bartkevicius (1996). Bergeat et al. (2001) and McDonald et al. (2012) estimated the effective temperature of BD+75 348 using the SED method of temperature calibration. Začs et al. (2000) derived the atmospheric parameters as well as abundances of 10 light and 9 heavy elements for BD+75 348. The literature values of $T_{\rm eff}$ for BD+75 348 range from 4700–4900 K. Our estimate of $T_{\rm eff}$ (∼4840 K) falls within the range. HE 0319–0215 and HE 0507–1653 are included in the list of faint high-latitude carbon stars of Christlieb et al. (2001). Goswami (2005) estimated the $^{12}C/^{13}C$ ratio for HE 0319–0215 ($^{12}C/^{13}C \sim 4.7$) and HE 0507–1653 ($^{12}C/^{13}C \sim 6.7$) based on medium-resolution spectra. From the studies of Hansen et al. (2016) on HE 0319–0215 and Hansen et al. (2016) and Jorissen et al. (2016) on HE 0507–1653 it is found that both objects exhibit radial velocity variations with periods of 3078 days for HE 0319–0215 and 405 days for HE 0507–1653 confirming their binary nature. Kennedy et al. (2011) derived the atmospheric parameters and abundance of oxygen for HE 0319–0215. Hansen et al. (2016) reported [Fe/H] = –2.30, [C/Fe] = 2.0, and [Ba/Fe] = 0.52 for HE 0319–0215. Karinkuzhi et al. (2021) also derived the atmospheric parameters and elemental abundances of HE 0319–0215 and reported the object as a CEMP-*r*/*s* star. However, the estimates of [Fe/H] and [Ba/Fe] by the studies of Hansen et al. (2016) and Karinkuzhi et al. (2021) differ by ∼0.6 dex and ∼1.23 dex, respectively. These discrepancies in the literature values compelled us to reinvestigate this object in detail using high-resolution spectroscopy. Schuler et al. (2008) reported [Fe/H] = –1.42, [C/Fe] = 1.33, and [N/Fe] = 1.20 for HE 0507–1653. Aoki et al. (2007) and Yong et al. (2013) derived the atmospheric parameters and abundances of C, N, Na, Mg, Ca, Sc, Ti, Cr, Ni, Zn, and Ba for HE 0507–1653. Karinkuzhi et al. (2021) reported this object as a CEMP-*s* star. However, this object also shows discrepancies in the atmospheric parameters and the abundance of Ba obtained by different groups. For instance, the ranges of $T_{\rm eff}$, log *g*, and [Fe/H] are 4880 to 5035 K, 1.50 to 2.40 dex, and –1.81 to –1.32 dex, respectively, and the [Ba/Fe] ranges from 1.56–1.89 dex. These differences prompted us to study this object in detail.

3. Source of Spectra

We acquired high-resolution spectra of BD+09 3019, BD +75 348, and HD 238020 using the Hanle Echelle SPectrograph (HESP) attached to the 2 m Himalayan Chandra Telescope (HCT) at the Indian Astronomical Observatory (IAO), Hanle. A 4K × 4K CCD detector with a pixel size of 15 μm is used. The wavelength of the spectra covers 3500–10 000 Å at a spectral resolution ($\lambda/\delta\lambda$) of 60,000. For data reduction, we have used Image Reduction and Analysis Facility (IRAF) software packages following a standard

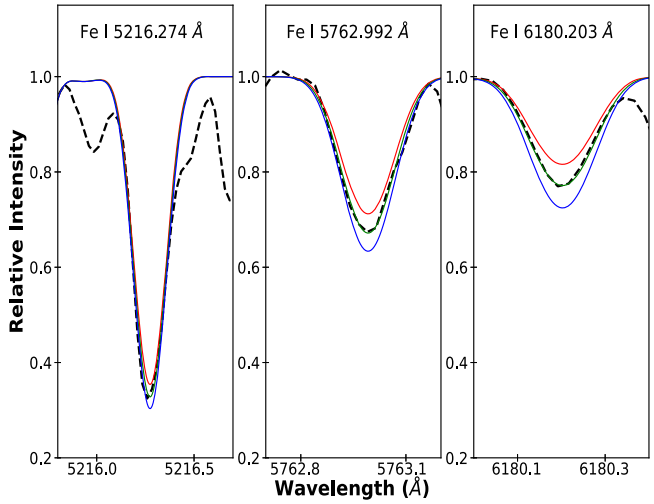

Figure 1. Spectral synthesis plots for a few Fe lines of the spectrum of HE 1023–1504.

procedure. We have applied spectroscopic data reduction procedures, such as trimming, bias subtraction, flat normalization, and extraction, to the raw data. A high-resolution Th-Ar arc spectrum is used for wavelength calibration. High-resolution spectra (R $\sim$ 50 000) of HE 0319–0215, HE 0507–1653, HE 0930–0018, and HE 1023–1504 are taken from the SUBARU archive[3] acquired using the High Dispersion Spectrograph (HDS; Noguchi et al. 2002) attached to the 8.2 m Subaru Telescope. For HE 0319–0215, HE 0930–0018, and HE 1023–1504, the wavelength coverage of the spectra spans from about 4020 to 6775 Å, with a gap of about 100 Å (from 5340 to 5440 Å). The wavelength coverage of the spectra of HE 0507–1653 spans from 4090 to 6870 Å, with a gap of 80 Å (from 5430 to 5510 Å). The gap in the wavelength coverage appears due to the physical spacing of the CCD detectors. We have continuum-fitted the spectra using the task continuum in IRAF. The sample spectra of the program stars in the wavelength region 5160–5190 Å are shown in Figure 2. The basic data for the program stars are presented in Table 1.

4. Photometric Temperatures

We have used broadband colors, optical, and IR to determine the photometric temperatures of the program stars with color–temperature calibrations, based on the infrared flux method (IRFM), available for main-sequence (Alonso et al. 1996) and giant stars (Alonso et al. 1999). We have taken the Two Micron All Sky Survey photometric magnitudes for J, H, and K from Cutri et al. (2003). We have followed the same procedure described in Goswami et al. (2006, 2015) and Goswami et al. (2021) as briefly outlined below. The photometric temperatures of the program stars corresponding to $J-H$ and $V-K$ colors are estimated at different assumed metallicity values. The estimated photometric temperatures are listed in Table 2. In order to select the model atmospheres to estimate the spectroscopic temperatures, we have used $T_{\rm eff}(J-K)$ as an initial guess as this temperature is independent of the metallicity (Alonso et al. 1996, 1999).

[3] http://jvo.nao.ac.jp/portal

5. Radial Velocities and Stellar Atmospheric Parameters

We have measured the radial velocities of the program stars using Doppler's formula from the shifts of the elemental absorption lines from the lab wavelengths. For this purpose, we have chosen a large number of clean and unblended spectral lines of different elements in each star and compared them with the rest-frame laboratory wavelength taking the spectra of Arcturus (Hinkle et al. 2000) as a template. As Arcturus belongs to the giant class and has a comparable temperature to those of the program stars, we have chosen Arcturus for the comparison to have homogeneity in the analysis. We have also used the FXCOR package in IRAF and cross-checked our measurements from line-to-line analysis to the measurements provided by FXCOR. The measured radial velocities, after correcting for heliocentric motion, and the standard deviations from the mean value are presented in Table 3, along with the radial velocity information provided by Gaia Collaboration et al. (2018). For the stars HE 0930–0018 and HE 1023–1504, radial velocities are not reported in Gaia Collaboration et al. (2018). However, the other five stars show significant differences between the radial velocities estimated by us and those of Gaia Collaboration et al. (2018), implying the possibility of the stars being part of a binary system with a now invisible companion.

Stellar atmospheric parameters, $T_{\rm eff}$, $\log g$, microturbulent velocity (ξ), and [Fe/H] are derived using the method described in Goswami et al. (2021), as briefly discussed below. For this analysis, we have chosen a set of clean and unblended Fe I and Fe II lines (Table 4) from each star. The excitation potentials of the lines range from 0.0 to 6.0 eV. The atomic line information is taken from the Kurucz atomic line database.[4] After strong filtration of the clean lines, we have considered (85, 12), (36, 3), (136, 17), (30, 5), (36, 4), (19, 3), and (20, 2) numbers of (Fe I, Fe II) lines in the spectra of BD+75 348, BD +09 3019, HD 238020, HE 0319–0215, HE 0507–1653, HE 0930–0018, and HE 1023–1504, respectively. For our analysis, we have used the code MOOG (Sneden 1973) in its updated 2013 version. MOOG assumes conditions of local thermodynamic equilibrium (LTE). We have selected the model atmospheres from the Kurucz grid of model atmospheres[5] with no convective overshooting, and the solar abundances are taken from Asplund et al. (2009). For determining the effective temperatures and microturbulent velocities of the program stars, we have used the conventional methods of excitation potential balance and equivalent width balance, respectively. The surface gravities of the program stars are determined by using the method of ionization equilibrium balance, in which the abundances of Fe measured from Fe I and Fe II lines are equated to fix the value of $\log g$. The abundances of Fe derived from Fe I and Fe II lines gives the metallicities of the stars. The atmospheric parameters of the program stars, along with the available literature values, are presented in Table 5.

6. Results

6.1. Abundance Analysis

We have determined the elemental abundances of the program stars by using an updated version of the code MOOG,

[4] https://lweb.cfa.harvard.edu/amp/ampdata/kurucz23/sekur.html
[5] http://kurucz.harvard.edu/grids.html

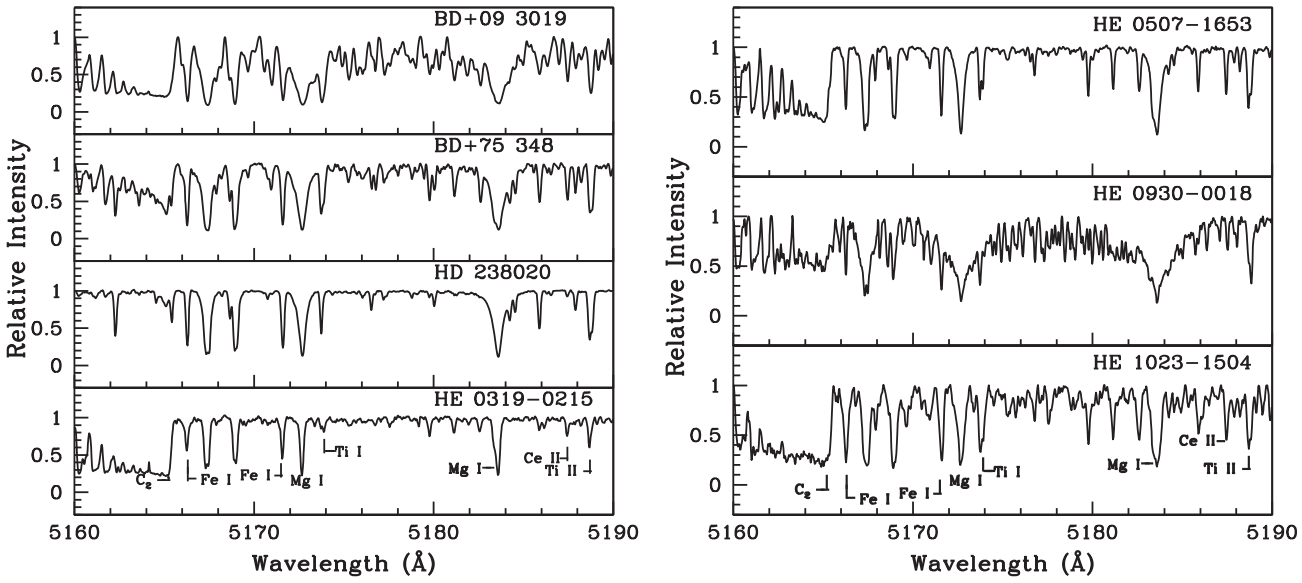

Figure 2. Sample spectra of the program stars in the wavelength region 5160–5190 Å.

which assumes LTE conditions. We have interpolated the model atmospheres to our derived stellar parameters from the Kurucz grid of model atmospheres, with no convecting overshooting, for the program stars. We have determined the abundances of light elements C, N, O, Na, Mg, Si, Ca, Sc, Ti, V, Cr, Mn, Co, Ni, Cu, and Zn and neutron-capture elements Sr, Y, Zr, Ba, La, Ce, Pr, Nd, Sm, Eu, Dy, and Hf for the program stars, depending upon the availability of the useful atomic lines or molecular bands of the elements. The abundances of C, N, O, and elements showing hyperfine splitting such as Sc, V, Mn, Ba, La, and Eu are determined using spectrum synthesis calculations. The abundances of the other elements are derived with the help of the equivalent width method by measuring the equivalent widths of clean and unblended spectral lines (Table 6) of the elements using the SPLOT task in IRAF. The atomic line information is taken from the Kurucz database of atomic line list. We have presented the abundance results in Tables 8 and 9.

6.1.1. C, N, O

The abundance of carbon is derived using three molecular bands of carbon, namely, the CH band around 4310 Å and the C_2 bands near 5165 and 5635 Å. Figure 3 shows the spectral synthesis of the C_2 molecular band around 5165 Å. The abundance of N is estimated from the CN molecular band around 4215 Å, adopting the carbon abundance derived using the C_2 and CH molecular bands. The abundance of oxygen could be determined only for HD 238020. We have used the [O I] 6300 Å forbidden line for estimating the abundance of oxygen.

For star HD 238020, the C_2 molecular band at 5635 Å and the CN molecular band are found to be too weak to be used for abundance estimation. In Figure 4 we show a comparison of the C_2 band at 5635 Å for stars BD+75 348, BD+09 3019, and HD 238020 to demonstrate the absence of the band in HD 238020. We could not use the CH molecular band in HE 0507–1653 and the CN molecular band in BD+09 3019 for abundance estimation as the bands are found to be saturated. For HE 0930–0018 and HE 1023–1504, the CH and CN molecular bands could not be used for abundance determination due to the low signal-to-noise ratio (S/N) in the particular region of the spectra (Figure 5). BD+09 3019, HE 0319–0215, HE 0507–1653, HE 0930–0018, and HE 1023–1504 are found to be carbon enhanced with [C/Fe] > 0.70. While BD+75 348 is mildly enhanced in carbon, the abundance of carbon in HD 238020 is found to be solar. Nitrogen is enhanced with [N/Fe] > 0.70 in all three stars (BD+75 348, HE 0319–0215, HE 0507–1653) for which the abundance of nitrogen could be estimated. The wavelengths, lower excitation potentials, and log *gf* values of different molecular transitions for the C_2 band at 5165 and 5635 Å and the CN band are adopted from Brooke et al. (2013), Ram et al. (2014), and Sneden et al. (2014). The molecular line list for the CH band at 4310 Å used for our calculation using *linemake*[6] (Placco et al. 2021) is from Masseron et al. (2014). The abundances of carbon derived from the different bands of C_2 and CH are found to be quite similar with a maximum difference of 0.16 dex for the star BD +09 3019. As shown in Goswami et al. (2021), the change in the abundance of C derived from the C_2 and CH bands varies in the ± 0.04 dex range with the change in temperature in the range ± 100 K. We observed negligible change in the abundance of C by varying $\log g$ and ξ by ± 0.2 (cgs) and ± 0.2 km s^{-1}, respectively. While the CH band shows a variation in the abundance of C by ± 0.04 dex with the metallicity variation in the range ± 0.2 dex, the C_2 bands show no variation.

6.1.2. Na, Mg, Si, Ca, Sc, Ti, V

The abundance of Na in the program stars ranges from [Na/Fe] $= 0.05$ to 0.95 dex, with the minimum [Na/Fe] for HD 238020 and the maximum for HE 0319–0215. Mg is moderately enhanced in all the program stars except for BD

[6] linemake contains laboratory atomic data (transition probabilities, hyperfine and isotopic substructures) published by the Wisconsin Atomic Physics and the Old Dominion Molecular Physics groups. These lists and accompanying line list assembly software have been developed by C. Sneden and are curated by V. Placco at https://github.com/vmplacco/linemake.

Table 1
Basic Data for the Program Stars

Star Name	R.A.(2000)	Decl.(2000)	*B*	*V*	*J*	*H*	*K*	Exposure (s)	Date of Obs.	Source of Spectrum	S/N (4000 Å)	S/N (6000 Å)
BD+75 348	08 46 11.64	+74 32 31.24	10.63	9.54	7.84	7.33	7.24	2400	08-03-2018	HESP/HCT	50	150
BD+09 3019	15 18 32.06	09 06 09.74	12.04	10.82	7.99	7.24	6.99	2700	24-05-2018	HESP/HCT	20	40
HD 238020	11 36 10.99	+56 50 17.66	9.34	8.49	6.90	6.51	6.38	1800	06-05-2017	HESP/HCT	70	200
HE 0319–0215	03 21 46.26	−02 04 33.95	15.03	13.60	11.79	11.22	11.06	1800	08-12-2003	HDS/SUBARU	40	70
HE 0507–1653	05 09 16.56	−16 50 04.69	13.63	12.51	10.88	10.43	10.32	1200	26-10-2002	HDS/SUBARU	40	75
HE 0930–0018	09 33 24.63	−00 31 44.60	16.13	14.70	12.19	11.55	11.34	1800	09-12-2003	HDS/SUBARU	10	30
HE 1023–1504	10 25 55.55	−15 19 17.08	16.26	14.40	12.32	11.61	11.42	1200	27-02-2005	HDS/SUBARU	7	25

Table 2
Temperatures from Photometry

Star Name	$T_{\rm eff}$ $(J-K)$	$T_{\rm eff}$ (-0.5) $(J-H)$	$T_{\rm eff}$ (-1.0) $(J-H)$	$T_{\rm eff}$ (-1.5) $(J-H)$	$T_{\rm eff}$ (-2.0) $(J-H)$	$T_{\rm eff}$ (-2.5) $(J-H)$	$T_{\rm eff}$ (-0.5) $(V-K)$	$T_{\rm eff}$ (-1.0) $(V-K)$	$T_{\rm eff}$ (-1.5) $(V-K)$	$T_{\rm eff}$ (-2.0) $(V-K)$	$T_{\rm eff}$ (-2.5) $(V-K)$	Spectroscopic estimates
BD+75 348	4856	4867	4891	4891	4867	4820	4749	4736	4729	4728	4733	4840
BD+09 3019	3879	4038	4051	4047	4027	⋯	3810	3795	⋯	⋯	⋯	4220
HD 238020	5085	5350	5382	5384	5358	5304	4941	4931	4928	4931	4941	5150
HE 0319–0215	4479	4616	4636	4635	4612	4568	4530	4517	4510	4510	4515	4650
HE 0507–1653	4935	5078	5105	5106	5081	5031	4855	4844	4839	4840	4848	4970
HE 0930−0018	4164	4354	4370	4368	4346	4306	4002	3988	3979	3974	⋯	4190
HE 1023–1504	4062	4144	4157	4154	4133	⋯	4211	4198	4190	4187	⋯	4440

Note. The numbers in the parenthesis below $T_{\rm eff}$ indicate the metallicity values at which the temperatures are calculated. Temperatures are given in Kelvin.

Table 3
Radial Velocities of the Program Stars

Star Name	V_r (Km s^{-1}) (Our estimates)	V_r (Km s^{-1}) (*a*)
BD+75 348	57.70 ± 1.72	56.91 ± 2.21
BD+09 3019	−9.50 ± 1.77	8.21 ± 0.65
HD 238020	−24.62 ± 3.07	−16.04 ± 0.15
HE 0319−0215	–257.43 ± 0.61	–232.33 ± 4.38
HE 0507–1653	349.81 ± 0.72	353.53 ± 2.55
HE 0930−0018	45.73 ± 0.68	⋯
HE 1023–1504	–226.15 ± 0.39	⋯

References: (*a*) Gaia Collaboration et al. (2018).

+09 3019, for which [Mg/Fe] = 1.26. We could estimate the abundance of Si only for HD 238020 using a single line Si I 6237.32 Å and found to be subsolar with [Si/Fe] = –0.52. This is somewhat surprising, as this object is classified as a mild Ba star with a probability of being a thin-disk object (see Section 6.2 for a kinematic analysis), and in the case of thin/thick-disk stars α-elements ([α/Fe]) are known to lie between 0.2 dex to 0.3 dex for stars with $-1.0 < [{\rm Fe/H}] < 0$ (Edvardsson et al. 1993). Within the metallicity range $-1.0 < [{\rm Fe/H}] < 0$, in barium stars [Si/Fe] is found to be in the range 0.0 dex to 0.58 dex (de Castro et al. 2016). Massive stars with masses $> 10\ M_{\odot}$ produce α-elements during hydrostatic oxygen burning and also during type II supernovae explosions (Woosley & Weaver 1986); hence Si is also expected to show a similar trend to that seen in other α-elements. Si is also known to show high scatter at all metallicities $-4 < [{\rm Fe/H}] < 0$. However, in metal-poor red horizontal-branch stars (i.e., BPS CS 22186–0005), [Si/Fe] is found to be as low as −0.25 dex (Preston et al. 2006), 0.27 dex higher than that observed in HD 238020. It will be worthwhile to investigate in the future the anomalous low Si abundance observed in HD 238020 that now remains unexplained. Ca is found to range from subsolar to super-solar abundances with $-0.14 < [{\rm Ca/Fe}] < 0.83$. The abundance of Sc is estimated using spectrum synthesis calculations of several Sc II lines (Table 7) whenever available. For five out of the seven objects, we have derived the abundance of Ti from the spectral lines of both the neutral (Ti I) and ionized (Ti II) species of Ti. The abundances of Ti derived from both the species are found to be very close for all the stars except for HE 0319–0215, with a difference of 0.14 dex. For BD+09 3019 and HE 1023–1504, the abundance of Ti could be derived only from Ti I lines as Ti I lines are found to be severely blended. The abundance of V is estimated from the spectrum synthesis calculation of V I line at 5727.652 Å (Table 7). We could only estimate an upper limit of V for object HE 0319–0215. The abundance of V ranges from subsolar to super-solar with $-0.39 < [{\rm V/Fe}] < 0.50$.

6.1.3. Cr, Mn, Co, Ni, Cu, Zn

For HD 238020, we could estimate the abundance of Cr from both neutral (Cr I) and ionized species (Cr II) of Cr. In other stars, we could not detect the lines due to Cr II, and the abundance could be derived only from Cr I lines. In the program stars, the abundance of Cr ranges from –0.51 dex to 0.11 dex. We have derived the abundance of Mn using spectrum synthesis calculation of several lines due to Mn I (Table 7). Mn is found to be subsolar in the program stars with $-1.33 < [{\rm Mn/Fe}] < -0.15$. For barium stars in the metallicity range $-1 < [{\rm Fe/H}] < 0.0$, [Mn/Fe] is found to lie in the range –0.55 dex to +0.37 dex (Yang et al. 2016; Shejeelammal et al. 2020). In our sample, the spectrum synthesis of the Mn I 4754.042 Å line in BD+09 3019, a strong barium star, returned a value of [Mn/Fe] = –1.33, making it the most Mn-deficient barium star. A few extremely metal-poor stars are however known to exhibit such low Mn abundances (i.e., HE 1012–1540, –1.00 dex; HE 1356–0622, –0.98 dex; Cohen et al. 2008). Lines due to Co, Cu, and Zn are not usable for abundance determination in HE 0319–0215. A few samples of these lines of this star are shown in Figure 6. For HE 1023–1504, we could not estimate the abundance of Cu due to the unavailability of good lines. In the other program stars Co ranges from subsolar to solar abundances with $-0.21 < [{\rm Co/Fe}] < 0.14$, Ni ranges from subsolar to super-solar abundances with $-0.30 < [{\rm Ni/Fe}] < 0.70$, [Cu/Fe] ranges from –0.20 dex to 0.38 dex, and [Zn/Fe] ranges from $-0.16 < [{\rm Zn/Fe}] < 0.13$.

6.1.4. Sr, Y, Zr

We could derive the abundance of Sr for all the stars except for HE 1023–1504. The Sr II 4215.52 Å line appears in the region of the CN molecular band around 4215 Å. This is why it is not always possible to use this particular line for objects with enhanced C and N abundances. We have used this line to estimate the abundance of Sr for HD 238020. For stars BD +75 348, HE 0319–0215, HE 0507–1653, and HE 0930–0018, the Sr I 4607.33 Å line (Table 7) is used for spectrum synthesis calculations. The abundance of Sr ([Sr/Fe]) in the program stars ranges from 0.08 dex to 1.67 dex. Y is found to be

Table 4
Equivalent Widths (in mÅ) of Fe lines Used for Deriving Atmospheric Parameters

Wavelength (Å)	Element	E_{low} (eV)	log gf	BD+75 348	BD+09 3019	HD 238020	HE 0319–0215	HE 0507–1653	HE 0930–0018	HE 1023–1504
4187.04	Fe I	2.45	−0.548	⋯	⋯	⋯	⋯	124.8 (6.12)	⋯	⋯
4202.03		1.48	−0.708	⋯	⋯	⋯	⋯	179.4 (6.02)	⋯	⋯
4203.57		1.01	−3.869	⋯	⋯	73.1 (6.72)	⋯	⋯	⋯	⋯

Note. The numbers in parentheses in columns 5–11 give the derived abundances from the respective line.

(This table is available in its entirety in machine-readable form.)

Table 5
Derived Atmospheric Parameters of our Program Stars and Literature Values

Star Name	$T_{\rm eff}$ (K)	log g (cgs)	ξ (km s^{-1})	[Fe I /H]	[Fe II/H]	[Fe/H]	Reference
BD+75 348	4840	2.00	1.43	−0.41 ± 0.20	−0.42 ± 0.18	−0.42	1
	4700	1.80	2.00	−0.86 ± 0.26	−0.88 ± 0.02	−0.87	9
	4900	…	…	…	…	…	8
	4760	…	…	…	…	…	10
BD+09 3019	4220	2.10	2.37	−0.55 ± 0.18	−0.54 ± 0.11	−0.55	1
HD 238020	5150	2.10	1.36	−0.67 ± 0.15	−0.68 ± 0.16	−0.68	1
	5035	…	…	…	…	…	8
HE 0319−0215	4650	0.50	1.33	−2.58±0.10	−2.56±0.05	−2.57	1
	4416	0.64	…	…	…	−2.42	2
	…	…	…	…	…	−2.30	3
	4738	0.66	2.16	…	…	−2.90	4
HE 0507–1653	4970	2.20	1.48	−1.46±0.11	−1.42±0.08	−1.44	1
	5000	2.40	2.00	−1.38±0.19	−1.39±0.17	−1.38	5
	…	…	…	…	…	−1.42	6
	4880	1.50	…	…	…	−1.81	2
	4935	1.88	…	…	…	−1.32	7
	5035	2.39	1.53	…	…	−1.35	4
HE 0930−0018	4190	2.65	1.86	−1.39±0.11	−1.39±0.09	−1.39	1
HE 1023–1504	4440	0.50	1.67	−1.66±0.14	−1.66±0.07	−1.66	1
	4421	0.66	…	…	…	−2.50	2

References: 1. Our work; 2. Kennedy et al. (2011); 3. Hansen et al. (2016); 4. Karinkuzhi et al. (2021); 5. Aoki et al. (2007); 6. Schuler et al. (2008); 7. Yong et al. (2013); 8. McDonald et al. (2012); 9. Začs et al. (2000); 10. Bergeat et al. (2001).

enhanced ([Y/Fe] > 0.70) in all the program stars except for HD 238020 (with [Y/Fe] = –0.26). For BD+75 348, HD 238020, and HE 0507–1653 we could estimate the abundance of Zr from lines due to both neutral (Zr I) and ionized (Zr II) species. The abundances of Zr derived from the lines of both species are very similar, with the largest difference of 0.25 dex for BD+75 348. The abundance of Zr ranges from 0.05 dex to 1.63 dex in the program stars.

6.1.5. Ba, La, Ce, Pr, Nd, Sm, Eu, Dy, Hf

The abundances of the neutron-capture elements are enhanced in all the program stars except for HD 238020. The abundances of Eu and Hf could not be estimated for HD 238020 as no lines could be detected. The abundances of Ba through Dy in HD 238020 are found to be moderately enhanced with 0.11 < [X/Fe] < 0.48.

The abundance of Ba is derived using spectral synthesis calculations of the Ba II 5853.668 and 6141.713 Å lines (Table 7) whenever available. The abundance of Ba could not be derived for BD+09 3019 as the Ba lines are found to be too strong and saturated. In the program stars, [Ba/Fe] ranges from 1.09 dex to 2.08 dex. The abundance of La is derived using spectrum synthesis calculation of the La II 4921.776 Å line (Table 7). La is found to be enhanced in the program stars with 1.09 < [La/Fe] < 2.25. [Ce/Fe] ranges from 1.34 dex to 2.50 dex in the program stars. The abundances of Pr, Nd, and Sm are enhanced ([X/Fe] > 0.90) in the program stars. The abundance of Eu is derived using spectrum synthesis calculations of Eu II 6437.640 and 6645.064 Å (Table 7). The abundance of Eu could not be derived for HE 0930–0018 as no Eu lines could be found in the spectrum (Figure 7). Eu is found to be enhanced ([Eu/Fe] > 0.70) in the rest of the program stars with 0.70 < [Eu/Fe] < 1.05. The abundance of Dy could be derived only for BD+75 348, BD+09 3019, and HD 238020, and the abundance of Hf could only be derived for BD+75 348.

6.2. Kinematic Analysis of the Program Stars

We have carried out a kinematic analysis of the program stars, following the procedure described in Purandardas et al. (2019) and Goswami et al. (2021), to know the Galactic population to which the program stars belong. The values of the parallax (π) and proper motions (μ_α, μ_δ) are taken from the Gaia database, and radial velocities of our estimates are considered for calculating the components of the space velocity ($U_{\rm LSR}$, $V_{\rm LSR}$, $W_{\rm LSR}$) with respect to local standard of rest (LSR). The total space velocity ($V_{\rm spa}$) is given by $V_{\rm spa}=\sqrt{U_{\rm LSR}^2 + V_{\rm LSR}^2 + W_{\rm LSR}^2}$. We have calculated the probabilities of the program stars being in the halo, thin disk, or thick disk using the procedures given by Reddy et al. (2006), Bensby et al. (2003, 2004), and Mishenina et al. (2004). For the probability determination, it is assumed that Gaussian distribution functions for $U_{\rm LSR}$, $V_{\rm LSR}$, and $W_{\rm LSR}$ with given mean values and dispersions represent the thin-disk, thick-disk, and halo populations (Reddy et al. 2006). A detailed discussion of the procedure can be found in our previous works (Purandardas et al. 2019; Goswami et al. 2021). The values of $U_{\rm LSR}$, $V_{\rm LSR}$, $W_{\rm LSR}$, $V_{\rm spa}$ and the probability estimates for the objects being members of the thin-disk ($P_{\rm thin}$), thick-disk ($P_{\rm thick}$), and halo ($P_{\rm halo}$) population are presented in Table 10. BD+75 348, HD 238020, and HE 0930–0018 show the probability of being thin-disk objects, BD+09 3019 is a thick-disk object, and HE 0319–0215 and HE 0507–1653 are halo objects. A Toomre diagram is shown in Figure 8.

7. Discussion

7.1. Classification Schemes of the Mild/strong Ba and CEMP-s Stars

7.1.1. Ba Stars

After the first identification of Ba stars by Bidelman & Keenan (1951), several authors (Pilachowski 1977; Sneden et al. 1981; Lu 1991; Jorissen et al. 1998; de Castro et al. 2016;

Table 6
Equivalent Widths (in mÅ) of Lines Used for the Calculation of Elemental Abundances

Wavelength (Å)	Element	E_{low} (eV)	log gf	BD+75 348	BD+09 3019	HD 238020	HE 0319–0215	HE 0507–1653	HE 0930–0018	HE 1023–1504
5682.633	Na I	2.10	−0.700	115.8 (6.25)	172.5 (6.08)	64.4 (5.62)	22.4 (4.71)	45.2 (5.19)	112.1 (5.39)	51.5 (5.06)
5688.205		2.10	−0.450	140.3 (6.42)	170.6 (5.81)	87.1 (5.77)	25.3 (4.53)	58.7 (5.17)	136.8 (5.43)	⋯
6154.23		2.10	−1.560	59.1 (6.14)	⋯	16.1 (5.50)	⋯	⋯	⋯	⋯
6160.75		2.10	−1.260	88.1 (6.30)	⋯	30.1 (5.55)	⋯	19.7 (5.21)	⋯	⋯

Note. The numbers in parentheses in columns 5–11 give the derived abundances from the respective line.

(This table is available in its entirety in machine-readable form.)

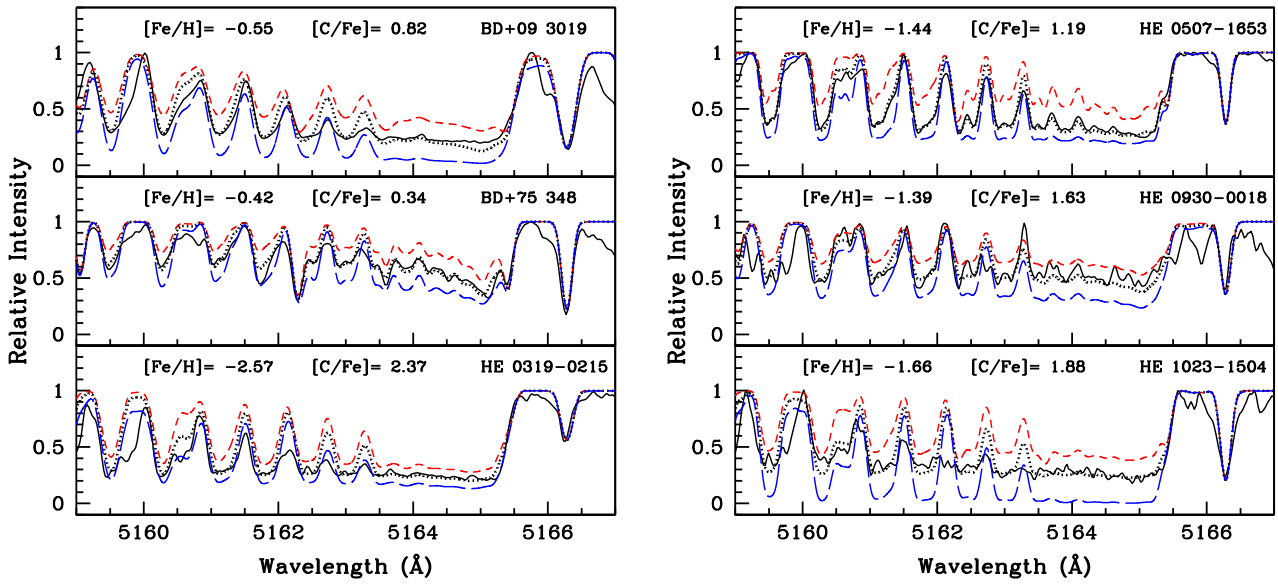

Figure 3. Spectral synthesis plot of the C_2 band around 5165 Å. The dotted lines indicate the synthesized spectra, and the solid lines indicate the observed spectra. Two alternative synthetic spectra are shown corresponding to Δ[C/Fe] = +0.3 (long-dashed line) and Δ[C/Fe] = −0.3 (short-dashed line).

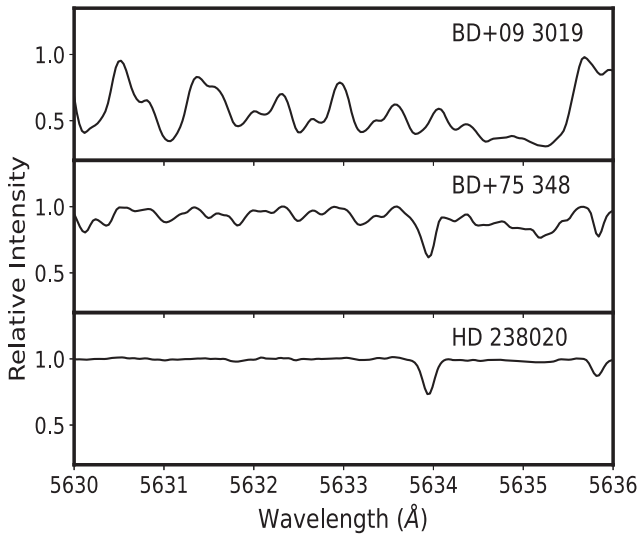

Figure 4. Sample spectra of the C_2 band at 5635 Å of the three Ba stars. This band is not present in star HD 238020.

Yang et al. 2016; Escorza et al. 2017; Jorissen et al. 2019) have put forward classification criteria to distinguish the mild and strong Ba stars. Pilachowski (1977) reported abundance analysis of seven mild Ba stars and demonstrated that they show [s/Fe] $\geqslant$ 0.50, where [s/Fe] implies the average abundance of the available *s*-process elements. Sneden et al. (1981) pointed out that the limiting values of [s/Fe] for mild Ba stars and classical (strong) Ba stars are 0.21 and 0.73, respectively. Using the Ba index given by Warner (1965), Lu (1991) classified Ba stars with Ba indexes of 0.3–1.5 and 2–5 as mild and strong Ba stars, respectively. Jorissen et al. (1998) classified stars with Ba $\leqslant$ 2 as mild and with Ba=3–5 as strong Ba stars. Escorza et al. (2017) considered stars with Ba indexes of 1 and 2 as mild Ba stars and of 3–5 as strong Ba stars. However, avoiding the use of Ba indices, Yang et al. (2016) used [Ba/Fe] as an indicator to distinguish the two groups. They considered stars showing [Ba/Fe] $>$ 0.60 as strong Ba stars. Their sample stars show 0.17 $<$ [Ba/Fe] $<$ 0.54 for mild Ba stars. de Castro et al. (2016) used [s/Fe] $\geqslant$ 0.25 as a distinguishing value between normal giants and Ba stars. Jorissen et al. (2019) recommended that [La/Fe] and [Ce/Fe] for strong Ba stars are greater than or equal to unity, and mild Ba stars always show [Ce/Fe] $\geqslant$ 0.2.

In this study, we use a similar criterion to that of Yang et al. (2016). However, as abundance of Ba is not reported for many Ba stars in the literature due to the saturation of strong Ba lines in the spectra of Ba stars, we use [hs/Fe] to differentiate between mild and strong Ba stars. Here, hs (heavy-s) represents Ba, La, Ce, and Nd. We have not used Pr and Sm in the calculations of hs, as the *r*-process contributes more to these two elements than the *s*-process. In order to reduce the systematic error in calculating [hs/Fe], we have considered only those stars for which abundances of at least two or more heavy-*s* process elements are reported in the literature. We consider stars with [hs/Fe] $>$ 0.60 as strong Ba stars and stars with 0.17 $<$ [hs/Fe] $<$ 0.60 as mild Ba stars. We have discarded the possibility of using [s/Fe] as a classifier, because [s/Fe] contains not only Pr and Sm, but also the ls elements Sr, Y, and Zr, and the *s*-process AGB models cannot satisfactorily reproduce the ls elements. These elements are believed to have contributions from several different sources.

7.1.2. *CEMP*-s *Stars*

CEMP stars are metal-poor stars ([Fe/H] $<$ –1.0) with [C/Fe] $>$ 0.7. Several classification schemes have been proposed in the literature (Beers & Christlieb 2005; Jonsell et al. 2006; Masseron et al. 2010; Abate et al. 2016; Frebel 2018; Hansen et al. 2019; Goswami et al. 2021) to identify the CEMP-*s* stars from the different subclasses of CEMP stars. However, it is difficult to distinguish between CEMP-*s* and CEMP-*r*/*s* stars (see Goswami et al. 2021, for more details). Beers & Christlieb (2005) for the first time used [Ba/Fe], [Eu/Fe], and [Ba/Eu] to differentiate between CEMP stars. Following this study, Jonsell et al. (2006), Masseron et al. (2010), and Abate et al. (2016)

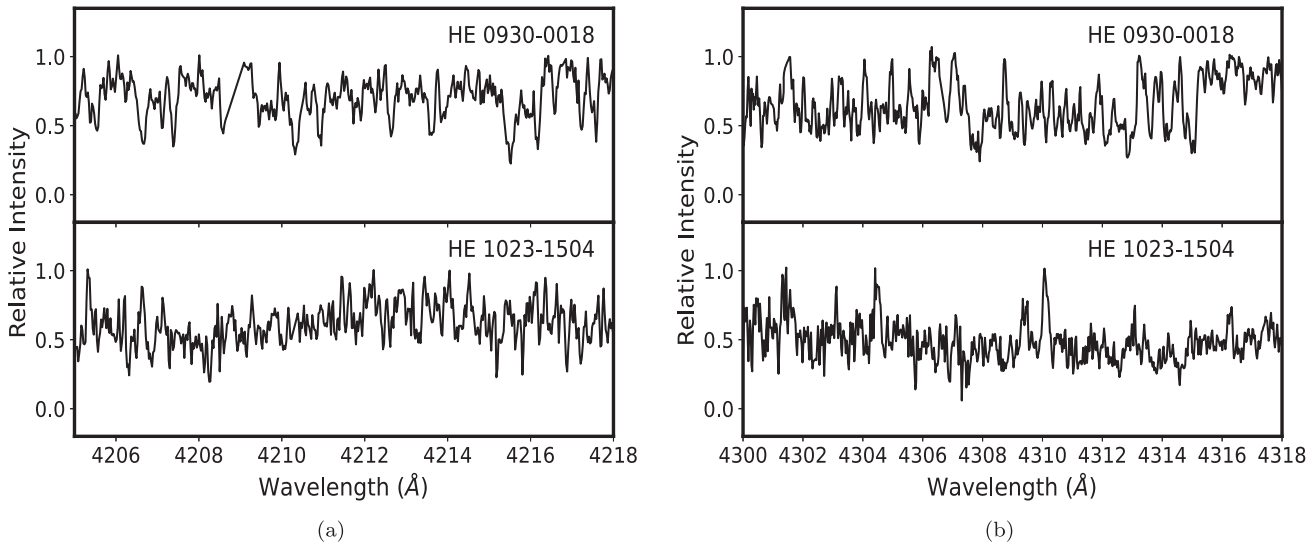

Figure 5. Sample spectra of HE 0930–0018 and HE 1023–1504 in the wavelength regions 4205–4218 Å and 4300–4318 Å.

Table 7
Absolute Abundances (log ϵ) Derived from Different Lines Using Spectral Synthesis Calculations

Wavelength (Å)	Element	BD+75 348	BD+09 3019	HD 238020	HE 0319–0215	HE 0507–1653	HE 0930–0018	HE 1023–1504	Reference
4415.557	Sc II	⋯	⋯	2.65	0.55	⋯	⋯	⋯	1[a]
5031.021		⋯	⋯	2.50	⋯	⋯	⋯	⋯	1[a]
5526.790		2.85	⋯	2.47	⋯	⋯	⋯	⋯	1[a]
5641.001		2.72	3.15	2.30	⋯	1.75	⋯	1.55	1[a]
5657.896		2.62	3.15	2.60	⋯	1.71	1.65	⋯	1[a]
5667.149		2.65	⋯	2.30	⋯	⋯	1.50	⋯	1[a]
5727.652	V I	3.12	3.88	3.23	< 1.60	2.80	2.66	2.53	2[a]
4754.042	Mn I	4.55	3.55	4.62	2.15	3.75	⋯	3.28	3[a]
4762.367		4.60	⋯	4.56	⋯	⋯	3.15	⋯	3[a]
4823.524		4.60	⋯	4.62	⋯	⋯	⋯	⋯	3[a]
5853.668	Ba II	3.47	⋯	⋯	1.37	2.70	1.55	2.60	4
6141.713		3.29	⋯	1.75	1.60	2.90	2.20	⋯	4
4921.776	La II	2.60	2.80	0.90	0.25	1.60	0.80	1.30	5
6437.640	Eu II	⋯	⋯	⋯	⋯	0.10	⋯	⋯	6[a]
6645.064		0.80	1.02	⋯	−1.20	0.12	⋯	−0.25	7

Notes. Hyperfine splitting contributions are taken from the sources given in Column 10.
[a] *linemake*
References: 1. Lawler et al. (2019); 2. Lawler et al. (2014); 3. Den Hartog et al. (2011); 4. McWilliam (1998); 5. Jonsell et al. (2006); 6. Lawler et al. (2001); 7. Worley et al. (2013).

used the same abundance ratios with different limiting values. Hansen et al. (2019) used [Sr/Ba] to distinguish the subclasses. In this paper, we have followed the classification scheme discussed in Goswami et al. (2021)

1. CEMP: [C/Fe] $\geqslant$ 0.7
2. CEMP-*r*/*s*: [Ba/Fe] $\geqslant$ 1.0, [Eu/Fe] $\geqslant$ 1.0
   (a) 0.0 $\leqslant$ [Ba/Eu] $\leqslant$ 1.0 and/or 0.0 $\leqslant$ [La/Eu] $\leqslant$ 0.7
3. CEMP-*s*: [Ba/Fe] $\geqslant$ 1.0
   (a) [Eu/Fe] < 1.0, [Ba/Eu] > 0.0 and/or [La/Eu] > 0.5
   (b) [Eu/Fe] $\geqslant$ 1.0, [Ba/Eu] > 1.0 and/or [La/Eu] > 0.7

7.2. Classification of the Program Stars

7.2.1. BD+75 348, BD+09 3019, and HD 238020

From the visual inspection of the strong lines Sr II 4077 and Ba II 4554 Å, we classify these three objects as Ba stars. The [Fe/H] values of BD+75 348, BD+09 3019, and HD 238020 lie between –0.68 and –0.42. BD+75 348, with [C/Fe] ∼0.31, is not a carbon-enhanced star, but it shows enhancement in neutron-capture elements. BD+09 3019, with [C/Fe] ∼0.77, shows enhancement in carbon, and the neutron-capture elements are also strongly enhanced in the star. The high value of [hs/Fe] (> 0.60) put BD+75 348 and BD+09 3019 in the category of strong Ba stars. HD 238020, on the other hand, shows only mild enhancement in neutron-capture elements with a solar abundance of carbon. C/O of HD 238020 is greater than unity. With [hs/Fe] = 0.30, we classify this object as a mild Ba star.

7.2.2. HE 0319–0215, HE 0507–1653, HE 0930–0018, and HE 1023–1504

HE 0319–0215, HE 0507–1653, HE 0930–0018, and HE 1023–1504 are metal-poor (MP; [Fe/H] < –1.0) and

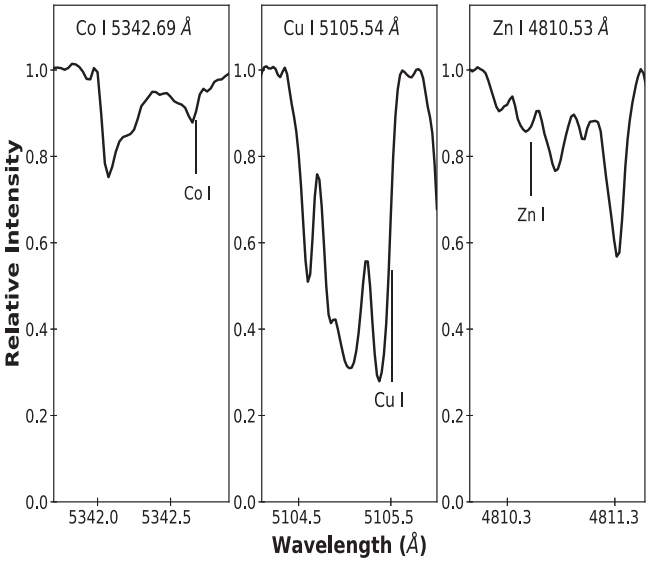

Figure 6. Sample spectra of the Co, Cu, and Zn lines of HE 0319–0215.

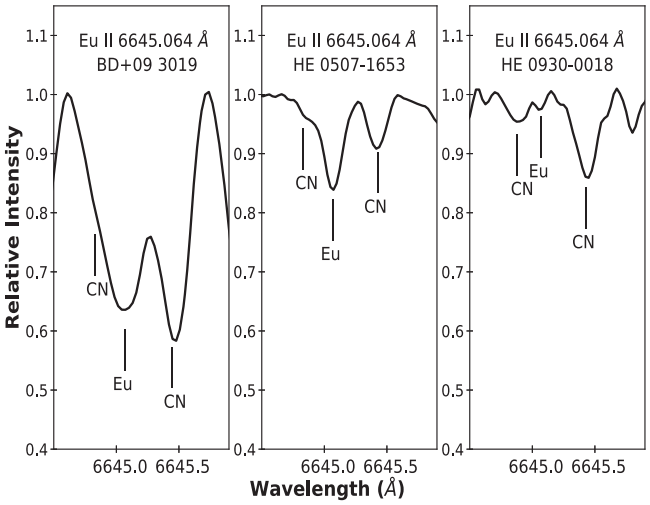

Figure 7. Sample spectra of the Eu II line at 6645.064 Å in stars BD+09 3019, HE 0507–1653, and HE 0930–0018. This line is very weak (not usable) in star HE 0930–0018.

very-metal-poor (VMP; [Fe/H] < –2.0) stars with –1.39 <[Fe/H] < –2.57. All these stars are carbon-enhanced ([C/Fe] > 1.0) and enriched in neutron-capture elements. All four stars fall in the category of CEMP-*s* stars following the classification criteria of Goswami et al. (2021). Although [Eu/Fe] is greater than unity in HE 0507–1653 and the classification scheme of Abate et al. (2016; Figure 9(a)) puts it in the category of CEMP-*r*/*s* stars based on [Ba/Eu] > 0.0, Figure 9(b) shows that this star is a CEMP-*s* star from the classification scheme of Goswami et al. (2021). We tried to fit *i*-process models (Hampel et al. 2016) calculated for neutron densities of $n \sim 10^9$–10^{15} cm^{-3} to the observed abundance pattern of HE 0507–1653. We found that the model with $n = 10^9$ cm^{-3} gives the minimum χ^2 value. So, this star cannot be a CEMP-*r*/*s* star. However, we will discuss in Section 7.4 that *s*-process yields produced by an $M = 2.0$ $M_\odot$ AGB can satisfactorily reproduce the observed abundance pattern of the star, placing it in the CEMP-*s* category. This verifies the upper limit on [Ba/Eu] (> 1.0) for CEMP-*r*/*s* stars put forward by our previous work (Goswami et al. 2021). Classifications of the program

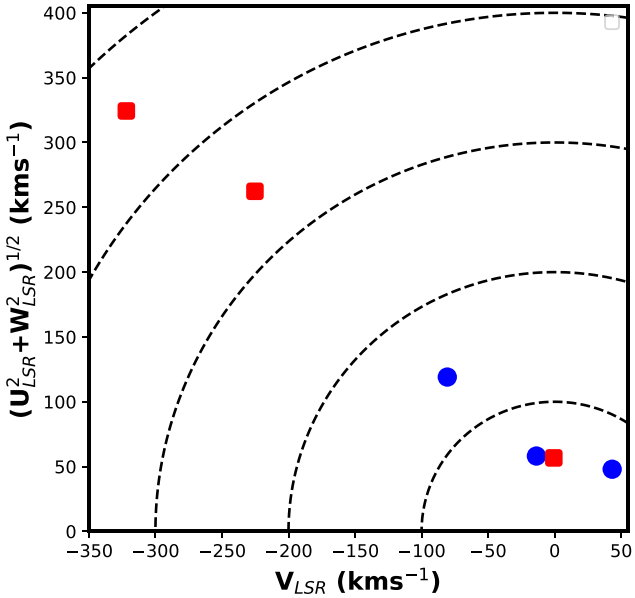

Figure 8. Toomre diagram. Red filled squares represent the CEMP-*s* stars, and blue filled circles represent Ba stars. The dashed curves connect the loci with same V_{LSR}.

stars along with some important abundance ratios, such as [ls/Fe], [hs/Fe], [hs/ls], [Eu/Fe], [Ba/Eu], and [La/Eu], are presented in Table 11.

7.3. Masses of the Program Stars

The masses of the program stars are estimated from the position of the stars on the Hertzprung–Russell (HR) diagram ($\log(L/L_\odot)$ versus $\log(T_{\rm eff})$ plot). In order to estimate the luminosities (L) of the program stars using Equation (1) the visual magnitudes (V) of the stars are taken from SIMBAD, the parallaxes (π) are taken from Gaia[7], the interstellar extinction (A_v) values are calculated from the formula given in Chen et al. (1998), and the bolometric corrections (BC) are calculated using the empirical calibrations of Alonso et al. (1999).

$$\log(L/L_\odot) = 0.4(M_{\rm bol\odot} - V - 5 - 5\log(\pi) + A_v - {\rm BC}). \quad (1)$$

We have used the updated BASTI-IAC evolutionary tracks[8] (Hidalgo et al. 2018) generated, including overshooting and diffusion, for the corresponding metallicities of the program stars. For $\log(T_{\rm eff})$, we have used our spectroscopic $T_{\rm eff}$ estimates. Figure 10(a) shows the appropriate evolutionary tracks corresponding to the Ba stars of our study. Figure 10(b) shows the evolutionary track corresponding to HE 0507–1653, a CEMP-*s* star of our study. We can see that the star falls toward the right side of the evolutionary track. This is because the evolutionary tracks highly depend on the opacity in the stellar atmospheres (Marigo 2002), and the BASTI-IAC evolutionary tracks are not calculated considering high carbon abundances. So, these evolutionary tracks are not suitable for carbon-enhanced stars. The use of the evolutionary tracks customized to the observed abundances of the stars is out of the scope of this paper. The masses of the program stars including $\log(L/L_\odot)$ estimates are presented in Table 12. Due to the

[7] https://gea.esac.esa.int/archive/
[8] http://basti-iac.oa-abruzzo.inaf.it/

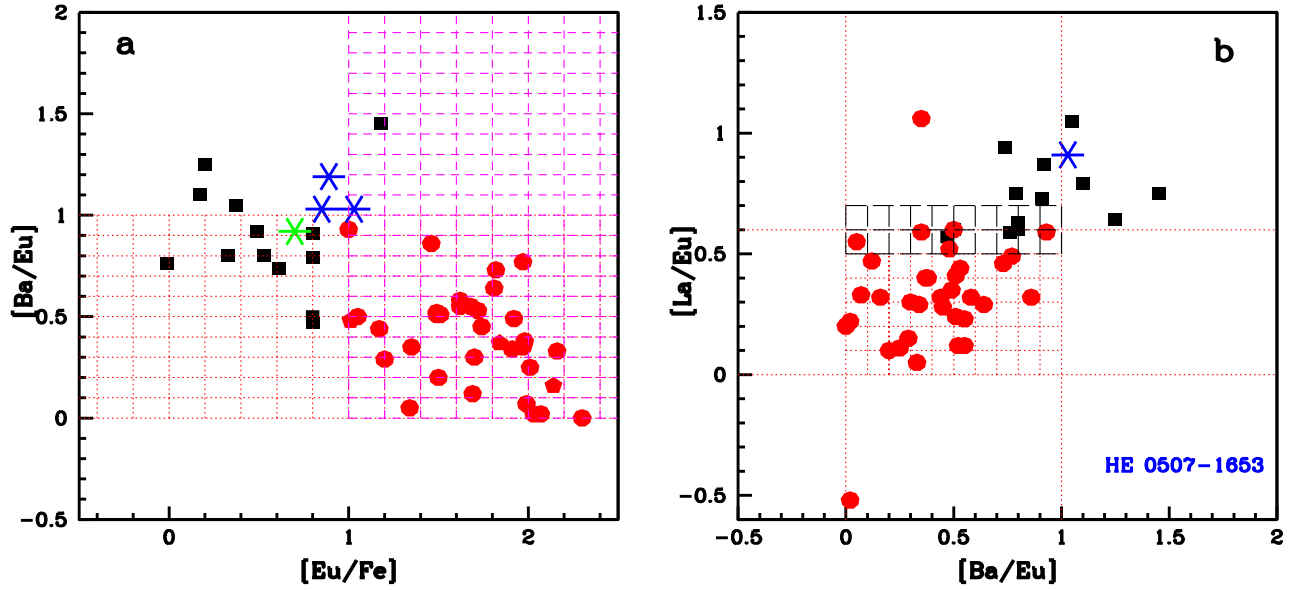

Figure 9. Filled red circles and filled black squares, respectively, represent literature CEMP-r/s and CEMP-s stars compiled by Goswami et al. (2021); blue and green stars represent the CEMP-s and Ba stars of this study. Panel (a): The grid formed by the dotted red lines represents the region of CEMP-r/s stars put forward by Beers & Christlieb (2005). The grid formed by the dashed magenta lines represents the region of CEMP-r/s stars put forward by Abate et al. (2016). Panel (b): The grid formed by the dotted red lines bound by $0.0 < [La/Eu] < 0.6$ and $0.0 < [Ba/Eu] < 1.0$ indicates the region defined for CEMP-r/s stars by Goswami et al. (2021). The grid formed by the black dashed lines bound by $0.5 < [La/Eu] < 0.7$ represents the region where $[Eu/Fe] > 1.0$ classifies the stars as CEMP-r/s and $[Eu/Fe] < 1.0$ classifies the stars as CEMP-s.

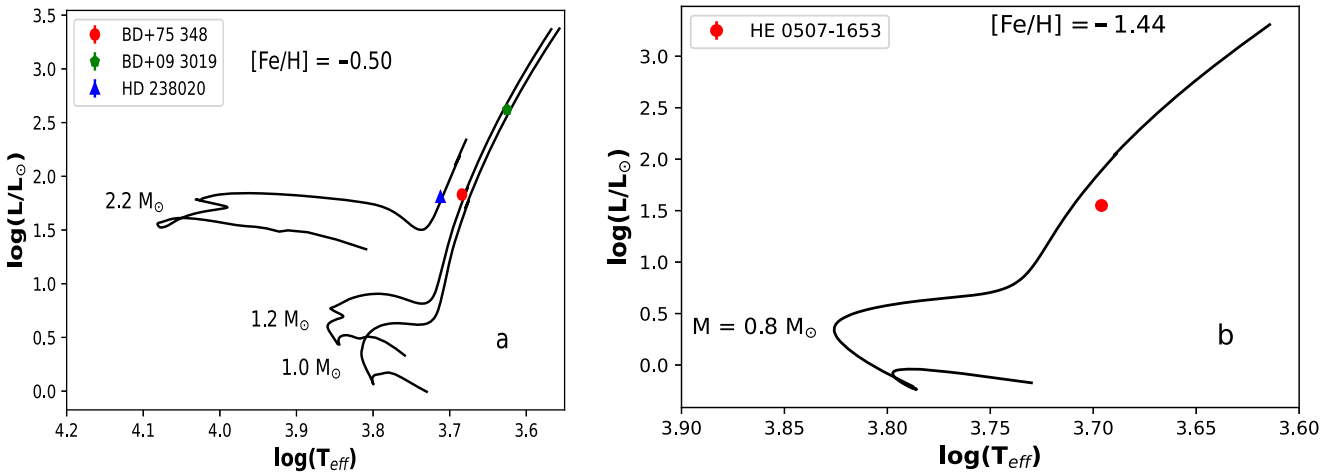

Figure 10. Hertzsprung–Russel diagram. Panel (a) shows the evolutionary tracks for different masses at [Fe/H] ∼–0.50. The red filled circle, green filled pentagon, and blue filled triangle represent the positions of the Ba stars of our study. In panel (b), an evolutionary track for $M = 0.8\ M_{\odot}$ at [Fe/H] = –1.44 is shown. The red filled circle represents a CEMP-s star HE 0507–1653.

precise parallax values provided by Gaia, the uncertainties in the estimation of the luminosities are so small that we cannot even see the error bars in Figure 10. However, the evolutionary tracks are available at mass intervals of 0.1 $M_{\odot}$ and 0.5 $M_{\odot}$ for mass ranges of 0.8–3 $M_{\odot}$ and 3–6 $M_{\odot}$, respectively. So, we consider an uncertainty in mass of $\pm 0.05\ M_{\odot}$ and $\pm 0.25\ M_{\odot}$ for the mass ranges 0.8–3 $M_{\odot}$ and 3–6 $M_{\odot}$, respectively.

7.4. Initial Masses of the Binary Companion (Primary)

We have performed a parametric-model-based analysis, using AGB yields of the FRUITY[9] models (Straniero et al. 2006; Cristallo et al. 2009, 2011, 2015) to estimate the initial masses of the companions of the program stars. We have followed the procedure discussed in Shejeelammal et al. (2020). We have calculated the s-process yields, using FRUITY models, for different masses (1.3–6.0 $M_{\odot}$) corresponding to the metallicities of the program stars. The model yields are calculated considering the conditions of standard ^{13}C pockets (Cristallo et al. 2015) and not the initial rotational velocities of the AGB stars. The observed abundances of the neutron-capture elements of a program star are then fitted with the following parametric model function as discussed in Husti et al. (2009)

$$\left[\frac{X}{Fe}\right] = \log\left(10^{[X/Fe]^{ini}} \times (1 - 10^{-d}) + 10^{[X/Fe]^{AGB} - d}\right), \quad (2)$$

[9] http://fruity.oa-teramo.inaf.it/

Table 8
Elemental Abundances in BD+75 348, BD+09 3019 and HD 238020

Element	Z	solar log ϵ [b]	BD+75 348 log ϵ (dex)	BD+75 348 [X/H]	BD+75 348 [X/Fe]	BD+09 3019 log ϵ (dex)	BD+09 3019 [X/H]	BD+09 3019 [X/Fe]	HD 238020 log ϵ (dex)	HD 238020 [X/H]	HD 238020 [X/Fe]
C (C_2, 5165 Å)	6	8.43	8.35 (syn)	−0.08	0.34	8.70 (syn)	0.27	0.82	7.75 (syn)	−0.68	0.00
C (C_2, 5635 Å)	6	8.43	8.30 (syn)	−0.13	0.29	8.71 (syn)	0.28	0.83	…	…	…
C (CH, 4310 Å)	6	8.43	8.30 (syn)	−0.13	0.29	8.55 (syn)	0.12	0.67	7.68 (syn)	−0.75	−0.07
N (CN, 4215 Å)	7	7.83	8.20 (syn)	0.37	0.79	(saturated)	…	…	…	…	…
O I	8	8.69	…	…	…	…	…	…	8.09 (syn)	−0.60	0.08
Na I	11	6.24	6.28 ± 0.12 (4)	0.04	0.46	5.95 ± 0.20 (2)	−0.29	0.26	5.61 ± 0.11 (4)	−0.63	0.05
Mg I	12	7.60	7.38 ± 0.17 (4)	−0.22	0.20	8.31 (1)	0.71	1.26	7.29 ± 0.08 (4)	−0.31	0.37
Si I	14	7.51	…	…	…	…	…	…	6.31 (1)	−1.20	−0.52
Ca I	20	6.34	5.97 ± 0.21 (16)	−0.37	0.05	5.65 ± 0.00 (2)	−0.69	−0.14	5.83 ± 0.19 (21)	−0.51	0.17
Sc II[a]	21	3.15	2.71 ± 0.09 (4)	−0.44	−0.02	3.15 ± 0.00 (2)	0.00	0.55	2.47 ± 0.13 (6)	−0.68	0.00
Ti I	22	4.95	4.65 ± 0.20 (13)	−0.30	0.12	4.78 ± 0.19 (2)	−0.17	0.38	4.45 ± 0.11 (14)	−0.50	0.18
Ti II	22	4.95	4.65 ± 0.19 (10)	−0.30	0.12	…	…	…	4.40 ± 0.20 (22)	−0.55	0.13
V I[a]	23	3.93	3.12 (1)	−0.81	−0.39	3.88 (1)	−0.05	0.50	3.23 (1)	−0.70	−0.02
Cr I	24	5.64	5.23 ± 0.15 (7)	−0.41	0.01	4.85 ± 0.18 (3)	−0.79	−0.24	4.98 ± 0.12 (13)	−0.66	0.02
Cr II	24	5.64	…	…	…	…	…	…	5.01 (1)	−0.63	0.05
Mn I[a]	25	5.43	4.58 ± 0.02 (3)	−0.85	−0.43	3.55 (1)	−1.88	−1.33	4.60 ± 0.03 (3)	−0.83	−0.15
Fe I	26	7.50	7.09 ± 0.20 (85)	−0.41	…	6.95 ± 0.18 (36)	−0.55	…	6.83 ± 0.15 (136)	−0.67	…
Fe II	26	7.50	7.08 ± 0.18 (12)	−0.42	…	6.96 ± 0.11 (3)	−0.54	…	6.82 ± 0.16 (17)	−0.68	…
Co I	27	4.99	4.49 ± 0.10 (2)	−0.50	−0.08	4.23 (1)	−0.76	−0.21	4.30 ± 0.20 (4)	−0.69	−0.01
Ni I	28	6.22	5.77 ± 0.24 (12)	−0.45	−0.03	5.65 (1)	−0.57	−0.02	5.60 ± 0.21 (15)	−0.62	0.06
Cu I	29	4.19	3.66 (1)	−0.53	−0.11	3.62 (1)	−0.57	−0.02	3.89 (1)	−0.30	0.38
Zn I	30	4.56	4.12 (1)	−0.44	−0.02	3.87 (1)	−0.69	−0.14	3.75 ± 0.04 (2)	−0.81	−0.13
Sr I	38	2.87	3.40 (syn)	0.53	0.95	3.99 (1)	1.12	1.67	…	…	…
Sr II	38	2.87	…	…	…	…	…	…	2.27 (1)	−0.60	0.08
Y II	39	2.21	3.06 ± 0.16 (10)	0.85	1.27	3.52 ± 0.20 (2)	1.31	1.86	1.27 ± 0.12 (8)	−0.94	−0.26
Zr I	40	2.58	3.16 ± 0.08 (3)	0.58	1.00	2.98 ± 0.14 (3)	0.40	0.95	2.01 ± 0.06 (2)	−0.57	0.11
Zr II	40	2.58	3.41 ± 0.09 (3)	0.83	1.25	…	…	…	1.95 ± 0.04 (2)	−0.63	0.05
Ba II[a]	56	2.18	3.38 ± 0.13 (2)	1.20	1.62	…	…	…	1.75 (1)	−0.43	0.25
La II[a]	57	1.10	2.60 (1)	1.50	1.92	2.80 (1)	1.70	2.25	0.90 (1)	−0.20	0.48
Ce II	58	1.58	2.97 ± 0.20 (13)	1.39	1.81	3.07 ± 0.16 (3)	1.49	2.04	1.09 ± 0.11 (7)	−0.49	0.19
Pr II	59	0.72	2.17 ± 0.22 (5)	1.45	1.87	2.65 ± 0.15 (3)	1.93	2.48	0.50 ± 0.20 (2)	−0.22	0.46
Nd II	60	1.42	2.63 ± 0.18 (11)	1.21	1.63	2.81 ± 0.06 (2)	1.39	1.94	1.00 ± 0.25 (12)	−0.42	0.26
Sm II	62	0.96	2.08 ± 0.07 (3)	1.12	1.54	2.78 ± 0.16 (3)	1.82	2.37	0.70 ± 0.07 (4)	−0.26	0.42
Eu II[*]	63	0.52	0.80 (1)	0.28	0.70	1.02 (1)	0.50	1.05	…	…	…
Dy II	66	1.10	1.49 (1)	0.39	0.81	2.43 (1)	1.33	1.88	0.53 (1)	−0.57	0.11
Hf II	72	0.85	2.33 (1)	1.48	1.90	…	…	…	…	…	…

Notes.
[a] The abundance is derived using spectrum synthesis calculations.
[b] Asplund et al. (2009). Columns 4, 7, and 10 present the abundances (log ϵ) of the different elements along with the standard deviations (when more than one line is used to derive the abundance). The numbers inside parentheses in columns 4, 7, and 10 show the numbers of lines used for the abundance determination.

where $\left[\frac{X}{Fe}\right]$ is the abundance of the element X in the program star, $[X/Fe]^{ini}$ is the initial abundance (before mass transfer) of the element X in the program star, $[X/Fe]^{AGB}$ is the AGB yield of the element X, and d is the dilution factor and a free parameter here. We find the model that gives the best fit to the observational data by varying d for each set of AGB model yields with different masses. In order to find the best fit, we calculated χ^2 for each AGB model. The corresponding mass of the AGB model for which we get the minimum value of χ^2 is the required mass of the companion AGB of the program star. The best-fit models with the AGB masses, corresponding dilution factors, and minimum χ^2 values of the program stars are shown in Figure 11.

7.5. Mass Distribution of Primary and Secondary Stars

The mass distribution of Ba stars has been previously studied by several groups (Han et al. 1995; Mennessier et al. 1997; Jorissen et al. 1998; Escorza et al. 2017; Jorissen et al. 2019). Using the same procedures discussed in Section 7.3 and Section 7.4, we have evaluated the mass distributions of Ba stars (secondary stars) and the primaries (companion AGBs) of both Ba and CEMP-*s* stars. For this analysis, we have selected a sample of 228 Ba stars and 36 CEMP-*s* stars from several sources in the literature. The atmospheric parameters and elemental abundances of the Ba stars are collected from Allen & Barbuy (2006), de Castro et al. (2016), Yang et al. (2016), Karinkuzhi et al. (2018), and Shejeelammal et al. (2020). We have calculated the [hs/Fe] values for the sample of 228 Ba stars and removed the ones

Table 9
Elemental Abundances in HE 0319–0215, HE 0507–1653, HE 0930–0018, and HE 1023–1504

Element	Z	solar log ϵ [b]	HE 0319–0215			HE 0507–1653		HE 0930–0018			HE 1023–1504		
			log ϵ (dex)	[X/H]	[X/Fe]	log ϵ (dex)	[X/H]	[X/Fe]	log ϵ (dex)	[X/H]	[X/Fe]	log ϵ (dex)	[X/H]	[X/Fe]
C (C_2, 5165 Å)	6	8.43	8.23 (syn)	−0.20	2.37	8.18 (syn)	−0.25	1.19	8.67 (syn)	0.24	1.63	8.65 (syn)	0.22	1.88
C (C_2, 5635 Å)	6	8.43	8.29 (syn)	−0.14	2.43	8.12 (syn)	−0.31	1.13	8.70 (syn)	0.27	1.66	8.72 (syn)	0.29	1.95
C (CH, 4310 Å)	6	8.43	8.30 (syn)	−0.13	2.44	(saturated)	⋯	⋯	Low S/N	⋯	⋯	Low S/N	⋯	⋯
N (CN, 4215 Å)	7	7.83	7.33 (syn)	−0.50	2.07	7.80	−0.03	1.41	Low S/N	⋯	⋯	Low S/N	⋯	⋯
Na I	11	6.24	4.62 ± 0.12 (2)	−1.62	0.95	5.19 ± 0.02 (3)	−1.05	0.39	5.41 ± 0.03 (2)	−0.83	0.56	5.06 (1)	−1.18	0.48
Mg I	12	7.60	5.51 (1)	−2.09	0.48	6.68 ± 0.11 (3)	−0.92	0.52	6.69 (1)	−0.91	0.48	6.30 ± 0.05 (syn, 2)	−1.30	0.36
Ca I	20	6.34	4.49 ± 0.21 (4)	−1.85	0.72	5.30 ± 0.19 (8)	−1.04	0.40	5.34 ± 0.11 (6)	−1.00	0.39	5.51 ± 0.14 (3)	−0.83	0.83
Sc II[a]	21	3.15	0.55 (1)	−2.60	−0.03	1.73 ± 0.03 (2)	−1.42	0.02	1.58 ± 0.08 (2)	−1.57	−0.18	1.55 (1)	−1.60	0.06
Ti I	22	4.95	3.16 (1)	−1.79	0.78	3.88 ± 0.11 (3)	−1.07	0.37	3.46 ± 0.21 (7)	−1.49	−0.10	3.95 ± 0.15 (3)	−1.00	0.66
Ti II	22	4.95	3.30 ± 0.12 (3)	−1.65	0.92	3.85 ± 0.23 (8)	−1.10	0.34	3.45 ± 0.20 (4)	−1.50	−0.11	⋯	⋯	⋯
V I[a]	23	3.93	< 1.60 (1)	< −2.33	< 0.24	2.80 (1)	−1.13	0.31	2.66 (1)	−1.27	0.12	2.53 (1)	−1.40	0.26
Cr I	24	5.64	3.18 ± 0.19 (3)	−2.46	0.11	4.21 ± 0.15 (6)	−1.43	0.01	3.74 ± 0.16 (3)	−1.90	−0.51	3.98 ± 0.11 (2)	−1.66	0.00
Mn I[a]	25	5.43	2.15 (1)	−3.28	−0.71	3.75 (1)	−1.68	−0.24	3.15 (1)	−2.28	−0.89	3.28 (1)	−2.15	−0.49
Fe I	26	7.50	4.92 ± 0.10 (30)	−2.58	⋯	6.04 ± 0.11 (36)	−1.46	⋯	6.11 ± 0.11 (19)	−1.39	⋯	5.84 ± 0.14 (20)	−1.66	⋯
Fe II	26	7.50	4.94 ± 0.05 (5)	−2.56	⋯	6.08 ± 0.08 (4)	−1.42	⋯	6.11 ± 0.09 (3)	−1.39	⋯	5.84 ± 0.07 (2)	−1.66	⋯
Co I	27	4.99	⋯	⋯	⋯	3.52 (1)	−1.47	−0.03	3.49 ± 0.12 (2)	−1.50	−0.11	3.47 (1)	−1.52	0.14
Ni I	28	6.22	3.35 ± 0.05 (syn, 2)	−2.87	−0.30	4.76 ± 0.18 (4)	−1.46	−0.02	5.57 ± 0.16 (3)	−0.65	0.74	5.26 ± 0.18 (2)	−0.96	0.70
Cu I	29	4.19	⋯	⋯	⋯	2.55 (1)	−1.64	−0.20	2.85 (1)	−1.34	0.05	⋯	⋯	⋯
Zn I	30	4.56	⋯	⋯	⋯	3.21 (1)	−1.35	0.09	3.30 (1)	−1.26	0.13	2.74 (1)	−1.82	−0.16
Sr I	38	2.87	1.97 (syn)	−0.90	1.67	2.97 (syn)	0.10	1.54	2.37 (syn)	−0.50	0.89	⋯	⋯	⋯
Y II	39	2.21	0.79 ± 0.20 (2)	−1.42	1.15	1.97 ± 0.11 (6)	−0.24	1.20	1.52 ± 0.18 (3)	−0.69	0.70	1.67 ± 0.21 (2)	−0.54	1.12
Zr I	40	2.58	⋯	⋯	⋯	2.71 ± 0.09 (2)	0.13	1.57	1.57 (1)	−1.01	0.38	⋯	⋯	⋯
Zr II	40	2.58	0.63 (1)	−1.95	0.62	2.77 ± 0.21 (2)	0.19	1.63	⋯	⋯	⋯	2.23 (1)	−0.35	1.31
Ba II[a]	56	2.18	1.49 ± 0.12 (2)	−0.69	1.88	2.80 ± 0.10 (2)	0.62	2.06	1.88 ± 0.32 (2)	−0.30	1.09	2.60 (1)	0.42	2.08
La II[a]	57	1.10	0.25 (1)	−0.85	1.72	1.60 (1)	0.50	1.94	0.80 (1)	−0.30	1.09	1.30 (1)	0.20	1.86
Ce II	58	1.58	0.93 ± 0.02 (2)	−0.65	1.92	2.17 ± 0.09 (9)	0.59	2.03	1.53 ± 0.13 (3)	−0.05	1.34	2.42 ± 0.19 (3)	0.84	2.50
Pr II	59	0.72	0.03 (1)	−0.69	1.88	1.25 (1)	0.53	1.97	0.41 ± 0.09 (2)	−0.31	1.08	1.60 ± 0.11 (3)	0.88	2.54
Nd II	60	1.42	0.74 ± 0.22 (6)	−0.68	1.89	2.01 ± 0.15 (11)	0.59	2.03	0.96 ± 0.14 (8)	−0.46	0.93	1.91 ± 0.13 (5)	0.49	2.15
Sm II	62	0.96	0.19 ± 0.13 (4)	−0.77	1.80	1.60 ± 0.15 (4)	0.64	2.08	0.55 ± 0.20 (2)	−0.41	0.98	1.24 ± 0.14 (2)	0.28	1.94
Eu II[a]	63	0.52	−1.20 (1)	−1.72	0.85	0.11 ± 0.01 (2)	−0.41	1.03	⋯	⋯	⋯	−0.25 (1)	−0.77	0.89

Notes.
[a] The abundance is derived using spectrum synthesis calculations.
[b] Asplund et al. (2009). Columns 4, 7, 10, and 13 present the abundances (log ϵ) of the different elements along with the standard deviations (when more than one line is used to derive the abundance). The numbers inside parentheses in columns 4, 7, 10, and 13 show the numbers of lines used for the abundance determination.

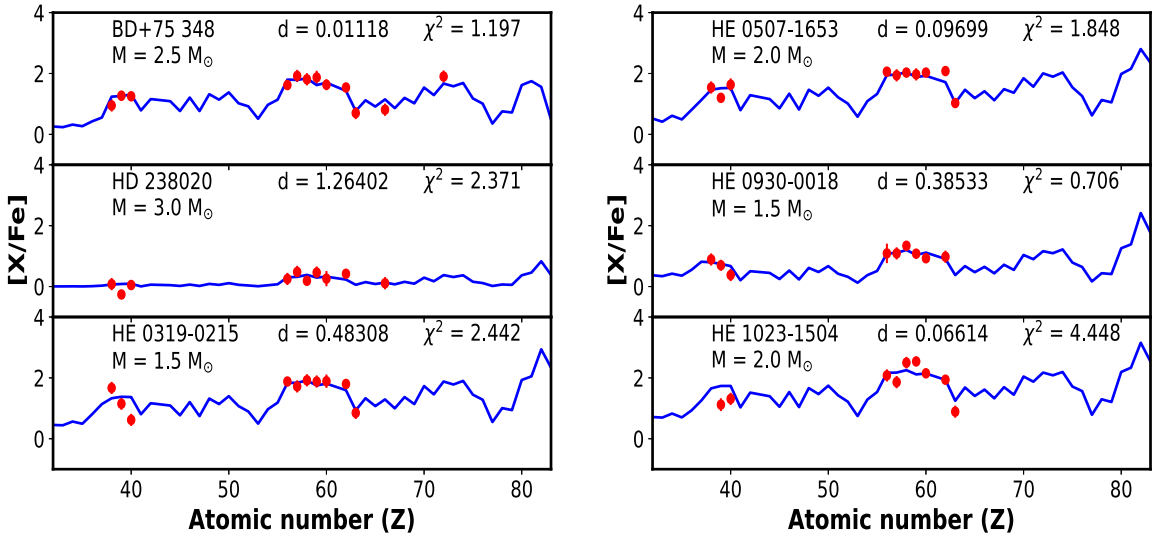

(a) (b)

Figure 11. Best-fit parametric models of the program stars. The points with error bars indicate the observed abundances.

Table 10
Spatial Velocity and Probability Estimates

Star Name	U_{LSR}(km s^{-1})	V_{LSR}(km s^{-1})	W_{LSR}(km s^{-1})	V_{spa}(km s^{-1})	P_{thin}	P_{thick}	P_{halo}
BD+75 348	–44.75±1.17	43.21 ± 0.93	17.28 ± 1.07	64.56 ± 0.10	0.97	0.03	0.00
BD+09 3019	102.34 ± 4.47	−80.69 ± 4.10	−60.85 ± 3.04	143.83 ± 0.41	0.00	0.97	0.03
HD 238020	–43.06 ± 1.41	−13.73 ± 1.02	−39.08 ± 2.60	59.75 ± 2.95	0.90	0.10	0.00
HE 0319−0215	305.94 ± 22.00	−321.86 ± 65.35	107.59 ± 16.06	456.91 ± 27.24	0.00	0.00	1.00
HE 0507−1653	–247.94 ± 1.03	−225.22 ± 2.55	−85.75 ± 3.89	345.76 ± 3.39	0.00	0.00	1.00
HE 0930−0018	–53.49 ± 0.42	−0.63 ± 0.47	18.80 ± 0.40	56.70 ± 0.27	0.98	0.02	0.00

Table 11
Observed Abundance Ratios and Classifications of the Program Stars

Star Name	[Fe/H]	[ls/Fe]	[hs/Fe]	[hs/ls]	[Eu/Fe]	[Ba/Eu]	[La/Eu]	Classification
BD+75 348	−0.42	1.16	1.75	0.59	0.70	0.92	1.22	Strong Ba star
BD+09 3019	−0.55	1.49	2.08	0.59	1.05	⋯	1.20	Strong Ba star
HD 238020	−0.68	–0.04	0.30	0.34	⋯	⋯	⋯	Mild Ba star
HE 0319–0215	−2.57	1.15	1.85	0.70	0.85	1.03	0.87	CEMP-*s* star
HE 0507–1653	−1.44	1.46	2.02	0.56	1.03	1.03	0.91	CEMP-*s* star
HE 0930–0018	−1.39	0.66	1.11	0.45	⋯	⋯	⋯	CEMP-*s* star
HE 1023–1504	−1.66	1.22	2.15	0.93	0.89	1.19	0.97	CEMP-*s* star

Table 12
Masses of the Program Stars

Star Name	Parallax (mas)	A_v	BC	log($L/L_\odot$)	log T_{eff}	Mass ($M_\odot$)
BD+75 348	1.6672 ± 0.0359	0.147608	−0.320606	1.83 ± 0.02	3.684	1.20
BD+09 3019	0.4105 ± 0.0183	0.000000	−0.690934	2.62 ± 0.04	3.625	1.00
HD 238020	2.4767 ± 0.0205	0.000000	−0.225678	1.81 ± 0.01	3.712	2.20
HE 0319–0215	0.0842 ± 0.0158	0.034626	−0.443833	2.80 ± 0.15	3.667	0.80

having [hs/Fe] $<$ 0.17. We believe that this lower limit (0.17) of [hs/Fe] will ensure the selection of true Ba stars from the sample. The sample of Ba stars ranges from [Fe/H] = –1.11 to +0.23. In Table 13, we have presented the list of Ba stars used for this study. Column 6 of Table 13 gives the [hs/Fe] that we have calculated and column 13 shows the classification. The atmospheric parameters and elemental abundances of CEMP-*s* stars are taken from our previously compiled CEMP-*s* stars' list in Goswami et al. (2021; Table 14). We could not estimate the masses of the sample of CEMP-*s* stars due to the inadequacy of the evolutionary tracks, as discussed in Section 7.3. Note that the method of

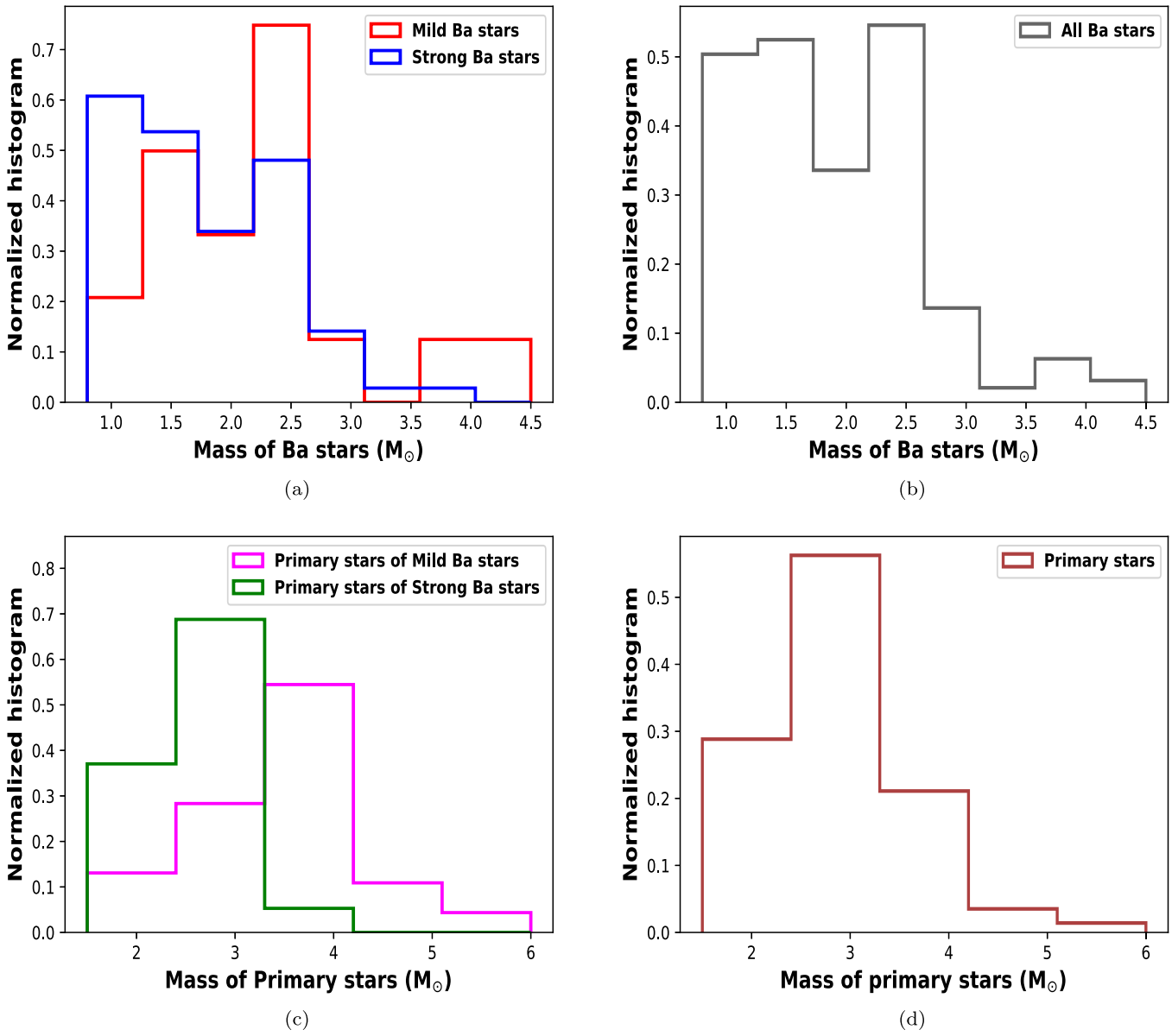

Figure 12. Mass distributions of Ba stars and their progenitor AGBs (primary stars). Panel (a) shows the mass distributions of mild and strong Ba stars. Panel (b) shows the mass distribution of both mild and strong Ba stars as a whole. Panel (c) shows the mass distributions of the primary stars of mild and strong Ba stars. Panel (d) shows the mass distribution of the primary stars of both mild and strong Ba stars as a whole.

Table 13
Masses of the Ba Stars and Initial Masses of their AGB Companions

Star Name	$T_{\rm eff}$ (K)	log g (cgs)	[Fe/H]	[ls/Fe]	[hs/Fe]	[hs/ls]	$M_{\rm Ba}$ ($M_\odot$)	$M_{\rm AGB}^{\rm ini}$ ($M_\odot$)	χ^2	dil	N	Type	Reference
BD-01302	4200	1.10	−0.64	-0.14	0.17	0.310	⋯	1.5	0.67	1.85697	5	m	1
BD-18821	5000	2.30	−0.27	0.70	1.27	0.570	2.30	3.0	1.92	0.18030	5	s	1
BD-083194	4900	3.00	−0.10	0.95	1.52	0.570	2.00	⋯	⋯	⋯	5	s	1

References: 1. de Castro et al. (2016).

(This table is available in its entirety in machine-readable form.)

deriving the masses of Ba and CEMP-*s* stars using evolutionary tracks in HR diagram has a serious drawback. The evolutionary tracks that we use do not take care of the mass transfer event taking place when the star is in the main-sequence stage.

7.5.1. Mass Distribution of Ba Stars

Han et al. (1995) from theoretical analysis showed that the average mass of strong Ba stars is expected to be about 1.8 $M_\odot$. They found a different peak (1.7 $M_\odot$) when all Ba stars, including mild and strong Ba stars, were considered.

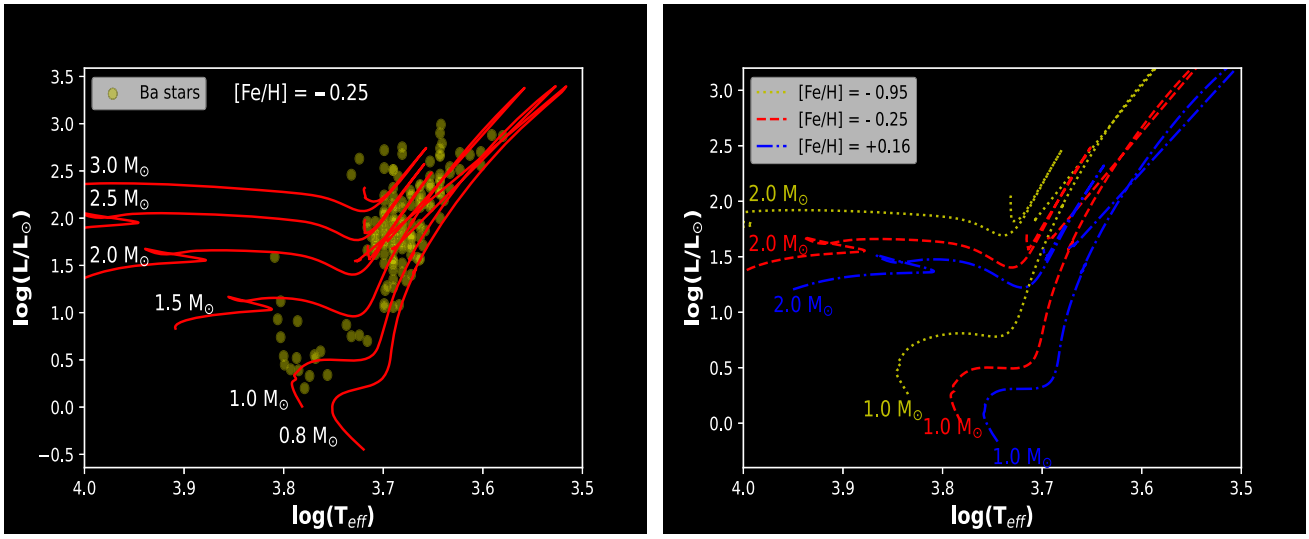

(a) (b)

Figure 13. Hertzsprung–Russel diagram. Panel (a) shows the evolutionary tracks for different masses at [Fe/H] = −0.25. Yellow points represent the positions of the Ba stars compiled from the literature. In panel (b), we have compared the evolutionary tracks for $M = 1.0\ M_{\odot}$ and $2.0\ M_{\odot}$ at three different metallicities [Fe/H] = –0.95, –0.25, and +0.16.

Mennessier et al. (1997) advocated that mild Ba stars are clump giants with a 2.5–4.5 $M_{\odot}$ mass range, and these stars are a population of high- and low-mass objects dominated by high-mass objects with a small tail of less massive objects. They found that strong Ba stars are giants in the mass range 1.0–3.0 $M_{\odot}$. Jorissen et al. (1998) also reported different mass values for mild and strong Ba stars. Supposing the mass of the companion white dwarf is $0.60 \pm 0.04\ M_{\odot}$, they estimated the masses of mild and strong Ba stars to be 1.90 ± 0.20 and 1.50 ± 0.20, respectively. Recently, Escorza et al. (2017) derived the mass distribution of Ba stars using a large sample. In order to find the masses of the Ba stars they generated the evolutionary tracks using STAREVOL at a metallicity of [Fe/H] = –0.25. They did not find any difference in the mass distribution of mild and strong Ba stars, unlike previous claims. They found that the mass distribution of Ba stars peak at 2.5 $M_{\odot}$ with a tail at higher masses up to 4.5 $M_{\odot}$. Jorissen et al. (2019) also presented the mass distribution of the Ba stars they studied using a similar method to that of Escorza et al. (2017), with the difference that they used the evolutionary tracks calculated at the metallicities of the individual stars. Jorissen et al. (2019) found that the masses of Ba stars range from 1.0–3.0 $M_{\odot}$ with a tail up to 5 $M_{\odot}$. This tail is comprised of mild Ba stars, mostly of [Fe/H] $\geqslant$ –0.1. Jorissen et al. (2019) mentioned that, in order to get the accurate mass distribution, it is important to use the evolutionary tracks corresponding to the metallicities of the respective stars.

Following the procedure described in Section 7.3 we have estimated the masses of the sample of Ba stars. We have used the BASTI-IAC evolutionary tracks at 11 different metallicities, [Fe/H] = +0.16, +0.05, –0.05, –0.15, –0.25, –0.35, –0.45, –0.55, –0.63, –0.72, and –0.95, covering the metallicity range of the sample. We could estimate the masses of 205 Ba stars in total, out of which 52 are mild Ba stars and 153 are strong Ba stars. The [Fe/H] and $T_{\rm eff}$ values of the stars are collected from the literature. The derived masses of the Ba stars are presented in Column 8 of Table 13. Similar to Escorza et al. (2017) and Jorissen et al. (2019), we also found that mild and strong Ba stars occupy the same mass range with the tails of strong and mild Ba stars going to $4.0 \pm 0.25\ M_{\odot}$ and $4.5 \pm 0.25\ M_{\odot}$, respectively (Figure 12(a)). Figure 13(a) shows the positions of the sample of Ba stars in the HR diagram with evolutionary tracks of different masses at [Fe/H] = –0.25. Figure 12(b) shows the whole sample of Ba stars without distinguishing between mild and strong Ba stars. We found that the mass distribution of the Ba stars cannot be explained by a single Gaussian distribution. Rather, Ba stars are distributed throughout the mass range with a disorderly manner. While Escorza et al. (2017) found the masses of Ba stars to peak at 2.5 $M_{\odot}$; in our case we found the average value of the distribution to be at 1.9 $M_{\odot}$. Note that Escorza et al. (2017) observed a lack of Ba stars in the mass range 1.0–2.0 $M_{\odot}$. However, neither our study nor the study by Jorissen et al. (2019) confirm that observation. The difference seen in this study and the study by Escorza et al. (2017) may come from two main sources. First, the evolutionary tracks used in the two studies are different. While Escorza et al. (2017) used the STAREVOL code to generate the evolutionary tracks, we have used the BASTI-IAC evolutionary tracks (see Figure 9 of Escorza et al. (2017) for a comparison of different sets of evolutionary tracks). Second, Escorza et al. (2017) estimated the masses using the evolutionary tracks of a single [Fe/H] (=–0.25) and our estimation is based on eleven different metallicities close to the

Table 14
Initial Masses of the AGB Companions of CEMP-*s* Stars

Star Name	$T_{\rm eff}$ (K)	log g (cgs)	[Fe/H]	$M_{\rm AGB}^{\rm ini}$ ($M_{\odot}$)	χ^2	dil.	N
BD+04 2466	5100	1.80	−1.92	3.0	3.61	0.26884	7
BS 16077-0077	5900	3.19	−2.05	2.0	1.89	1.14484	9
CD-27 14351	4320	0.50	−2.71	1.3	8.02	0.24628	8

(This table is available in its entirety in machine-readable form.)

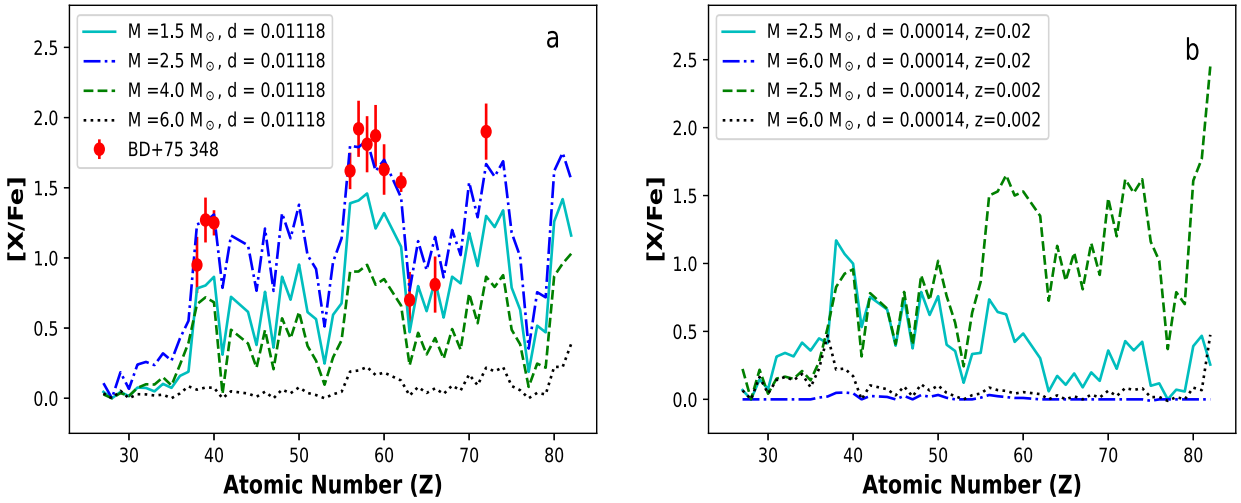

(a) (b)

Figure 14. Panel a: Comparison of the *s*-process AGB model yields obtained at $z = 0.006$ for different masses using the same dilution factor (d). The points with error bars indicate the observed abundances of BD+75 348. Panel b: Comparison of the *s*-process AGB model yields obtained at two metallicities $z = 0.02$ and $z = 0.002$ for two masses $M = 2.5$ and 6.0 $M_{\odot}$ using the same dilution factor (d).

metallicities of the sample stars. For instance, Figure 13(b) shows how different the evolutionary track of a particular mass can be at different metallicities.

7.5.2. Mass Distribution of Primary Stars

We have estimated the masses of the companion AGBs of the sample of Ba and CEMP-*s* stars following the same procedure as that described in Section 7.4. For this study, we assume that the enhancement of neutron-capture elements in all of these stars is due to a mass transfer event in a binary system where the slightly massive companion (primary star) evolves through the AGB phase, produces neutron-capture elements, and transfers the elements to the secondary star, which significantly alters the surface composition of the secondary star. If the uncertainty in the abundance for a particular element is not reported in the literature, we consider the uncertainty to be 0.2 dex. The number of neutron-capture elements for which abundance estimates are available in the literature range from 4 to 14 (column 12 of Table 13 and column 8 of Table 14).

Ba Stars: We could estimate the masses of the primary companions of 158 Ba stars. Out of these, 52 are mild Ba stars and 106 are strong Ba stars. We have divided the sample of Ba stars into seven groups based on the metallicities of the stars and used FRUITY models at $z = 0.020$, 0.014, 0.010, 0.008, 0.006, 0.003, 0.002. We have presented the initial masses of the primary stars ($M^{\rm ini}_{\rm AGB}$), χ^2, dilution factor (d), and number of elements used for the analysis (N) in columns 9, 10, 11, and 12, respectively, of Table 13. When we plot the histograms of the primary companions' masses for the mild and strong Ba stars separately, we can clearly see two peaks (Figure 12(c)). The mass range of primaries for mild Ba stars ($1.5 < M_{\odot} < 6.0$) is greater than that ($1.5 < M_{\odot} < 4.0$) of strong Ba stars. The masses of primaries of strong Ba stars peak at 2.5 $M_{\odot}$ with a standard deviation of 0.51 $M_{\odot}$ and those of mild Ba stars peak at 3.7 $M_{\odot}$ with a standard deviation of 1.03 $M_{\odot}$. If we consider the Ba star sample as a whole and not distinguish between mild and strong Ba stars, then the primaries of Ba stars peak at 2.9 $M_{\odot}$ with a standard deviation of 1.15 $M_{\odot}$ (Figure 12(d)). We note that Stancliffe (2021) studied the observed properties of the barium star sample of de Castro et al. (2016) considering models involving mass transfer from an AGB companion. The extent of dilution of accreted material as the star evolves has been examined, and its impact on the surface abundances is discussed. He could best-fit 32 objects from the sample using ejecta from 2.5 $M_{\odot}$ AGB stars and 36 objects using ejecta from 3 $M_{\odot}$ AGB stars. The accretion masses are found to be broadly consistent with the results obtained from hydrodynamical simulations of wind mass transfer in the binary systems of Liu et al. (2017).

CEMP-s Stars: The metallicities of the sample of 36 CEMP-*s* stars range from [Fe/H] = –3.00 to –1.29. We have divided the sample into five groups based on the metallicities of the stars. We have used FRUITY models at $z = 0.001$, 0.0003, 0.0001, 0.00005, 0.00002. We have presented the initial masses of the primary stars ($M^{\rm ini}_{\rm AGB}$), χ^2, dilution factor (d), and number of elements used for the analysis (N) in columns 5, 6, 7, and 8, respectively, of Table 14. The primary mass distribution of CEMP-*s* stars peaks at 2.03 $M_{\odot}$ with a standard deviation of 0.49 $M_{\odot}$ (Figure 16).

7.6. Formation Scenarios of Mild and Strong Ba Stars

de Castro et al. (2016) considered that mild Ba stars are formed from interstellar matter that is mildly enhanced with *s*-process elements. However, studies (Jorissen et al. 1998, 2019) have shown that both mild and strong Ba stars are formed in binary systems, and AGB mass transfer is responsible for the enhanced abundances of heavy elements. So, we can safely discard this formation scenario. From theoretical analysis, Han et al. (1995) showed that, while most mild Ba stars are formed by the wind accretion and wind exposure channels, strong Ba stars are formed by the wind accretion, wind exposure, and stable Roche lobe overflow (RLOF) channels. Yang et al. (2016) discussed two possible formation scenarios for the formation of mild Ba stars: (i) the mild enhancement could be explained by weaker neutron exposure in the progenitor AGB, and/or (ii) less accretion efficiency due to a longer orbital period, which means a larger distance between the binary companions. However, from long-term radial velocity

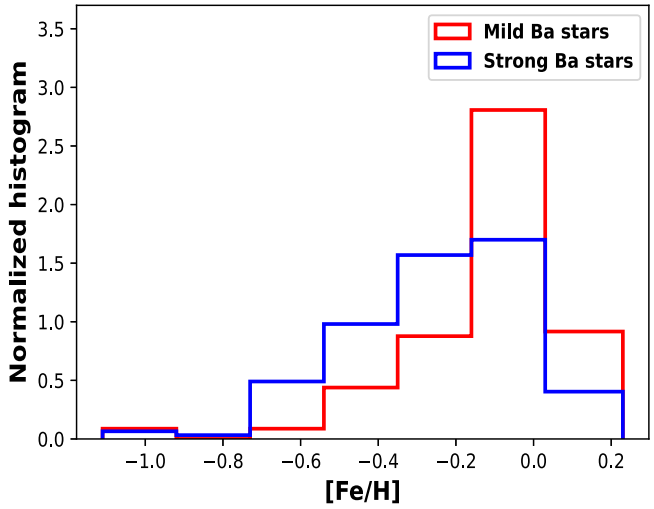

Figure 15. Metallicity distribution of the sample of mild and strong Ba stars.

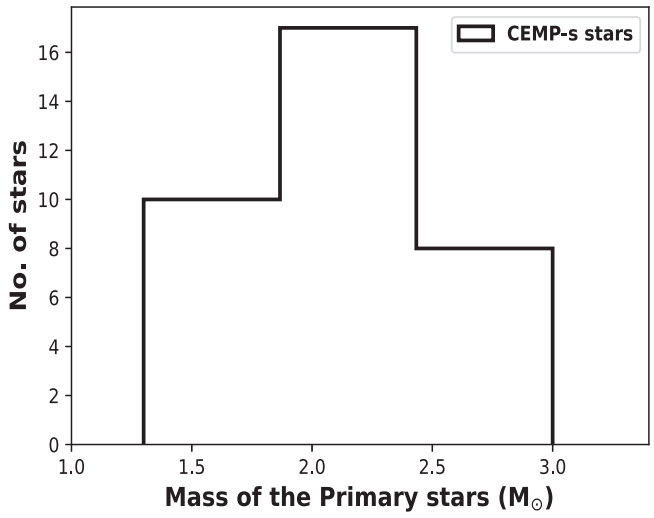

Figure 16. Mass distribution of the primary companions of the CEMP-*s* stars.

monitoring programs, Jorissen et al. (1998, 2019) have shown that mild Ba stars are not limited to long-period systems only. The orbital periods of strong Ba stars are generally shorter than those of mild Ba stars, but there is no tight correlation. In fact, there is a clear overlap in the orbital periods of these two subclasses. From Table 8 of Jorissen et al. (2019), we can see that the period ranges of mild and strong Ba stars are 80–22065 days and 185.7–8523 days, respectively. So, a scenario adopting a longer orbital period cannot explain the formation of a mild Ba star. However, we note that the ranges of both orbital periods and progenitor masses of mild Ba stars are larger than those of strong Ba stars.

The difference in the peaks of primaries for mild and strong Ba stars (Figure 12(c)) indicates that companions of mild Ba stars are more massive than those of strong Ba stars. This is not surprising because, from Figure 14(a), it can be seen that massive (e.g., 4, 5, 6 $M_{\odot}$) AGBs yield less than the low-mass AGBs with same dilution factor. So, we can say that the dominant factor controlling the abundance peculiarities of mild Ba stars is the initial mass of the companion. Mass transfer from 4.0–6.0 $M_{\odot}$ AGB companions can describe the formation of mild Ba stars. The white dwarf masses of $\sim$1.0 $M_{\odot}$ around Ba stars also point toward a massive (5 $M_{\odot}$) companion AGB (Jorissen et al. 2019). However, there is an overlap from 1.3–4.0 $M_{\odot}$ in the case of primary masses of mild and strong Ba stars. In this mass range, the metallicity of the system and dilution (hence the distance of the binary companions) play crucial roles to the formation of mild Ba stars. From Figure 15, we see that the mild Ba stars are distributed toward higher metallicities compared to strong Ba stars, and Figure 14(b) shows the metallicity dependence of the AGB models. At higher metallicities, *s*-process efficiency decreases and hence AGB yields decrease.

8. Conclusions

We have conducted detailed spectroscopic analysis of seven stars based on high-quality, high-resolution spectra. Out of the seven program stars, we have classified two stars (BD +09 3019 and BD+75 348) as strong Ba stars, one star (HD 238020) as a mild Ba star, and the other four stars (HE 0319–0215, HE 0507–1653, HE 0930–0018, and HE 1023–1504) as CEMP-*s* stars. Note that HE 0507–1653 shows [Eu/Fe] > 1.0 and according to the classification criteria of Abate et al. (2016) this star belongs to the category of CEMP-r/s stars, but the classification criteria that we proposed in Goswami et al. (2021) place this star in the CEMP-*s* subclass. While we could not obtain a reasonable fit for this object with *i*-process models with higher ($\geqslant 10^{12-15}$ cm^{-3}) neutron densities, the *s*-process AGB model with initial mass 2.0 $M_{\odot}$ satisfactorily reproduces the observed abundance pattern. Kinematic analysis shows that BD+75 348, HD 238020, and HE 0930–0018 belong to the thin-disk population, BD+09 3019 is a thick-disk object, and HE 0319–0215 and HE 0507–1653 show the probability of being halo objects.

We have derived the mass distribution of Ba stars and found that a single Gaussian cannot describe the mass distribution. The average mass of the distribution is found to be 1.9 $M_{\odot}$ with the tails of strong and mild Ba stars going up to 4.0 $M_{\odot}$ and 4.5 $M_{\odot}$, respectively. We confirm the previous claim by Escorza et al. (2017) that mild and strong Ba stars occupy the same mass range, but we do not confirm their claim that there is a lack of Ba stars in the mass range 1.0–2.0 $M_{\odot}$. Using parametric-model-based analysis we have derived the mass distributions of the AGB progenitors of the Ba and CEMP-*s* stars. To the best of our knowledge, this is the first attempt to derive the initial mass distributions of the primary companions of these stars. We found that the mass distributions of the progenitor AGBs of the mild and strong Ba stars peak at different values. The peaks of the progenitor mass distributions of mild and strong Ba stars are at 3.7 $M_{\odot}$ and 2.5 $M_{\odot}$, respectively. We can, therefore, say that the initial mass of the companion AGB is the dominant factor controlling the heavy elements' enhancement in mild Ba stars. However, we cannot neglect the orbital periods and metallicities of the binary systems as clear overlap can be seen in the progenitor mass distributions and orbital periods of mild and strong Ba stars. The mass distribution of the progenitor AGBs of CEMP-*s* stars peak at 2.03 $M_{\odot}$ with a standard deviation of 0.49 $M_{\odot}$.

This work made use of the SIMBAD astronomical database, operated at CDS, Strasbourg, France; the NASA ADS, USA; and data from the European Space Agency (ESA) mission Gaia

(https://www.cosmos.esa.int/gaia), processed by the Gaia Data Processing and Analysis Consortium (DPAC; https://www.cosmos.esa.int/web/gaia/dpac/consortium). We thank the referee for useful comments and suggestions. We are thankful to Melanie Hampel for providing us with the *i*-process yields in the form of number fractions. Funding from DST SERB project No. EMR/2016/005283 is gratefully acknowledged.

ORCID iDs

Partha Pratim Goswami https://orcid.org/0000-0002-5081-3208
Aruna Goswami https://orcid.org/0000-0002-8841-8641

References

Abate, C., Stancliffe, R. J., & Liu, Z.-W. 2016, A&A, 587, A50
Allen, D. M., & Barbuy, B. 2006, A&A, 454, 895
Alonso, A., Arribas, S., & Martinez-Roger, C. 1996, A&A, 313, 873
Alonso, A., Arribas, S., & Martínez-Roger, C. 1999, A&AS, 140, 261
Aoki, W., Beers, T. C., Christlieb, N., et al. 2007, ApJ, 655, 492
Asplund, M., Grevesse, N., Sauval, A. J., & Scott, P. 2009, ARA&A, 47, 481
Banerjee, P., Qian, Y.-Z., & Heger, A. 2018, ApJ, 865, 120
Bartkevicius, A. 1996, BaltA, 5, 217
Beers, T. C., & Christlieb, N. 2005, ARA&A, 43, 531
Bensby, T., Feltzing, S., & Lundström, I. 2003, A&A, 410, 527
Bensby, T., Feltzing, S., & Lundström, I. 2004, A&A, 415, 155
Bergeat, J., Knapik, A., & Rutily, B. 2001, A&A, 369, 178
Bidelman, W. P., & Keenan, P. C. 1951, ApJ, 114, 473
Brooke, J. S. A., Bernath, P. F., Schmidt, T. W., & Bacskay, G. B. 2013, JQRST, 124, 11
Chen, B., Vergely, J. L., Valette, B., & Carraro, G. 1998, A&A, 336, 137
Christlieb, N., Green, P. J., Wisotzki, L., & Reimers, D. 2001, A&A, 375, 366
Cohen, J. G., Christlieb, N., McWilliam, A., et al. 2008, ApJ, 672, 320
Cowan, J. J., & Rose, W. K. 1977, ApJ, 212, 149
Cristallo, S., Piersanti, L., Straniero, O., et al. 2009, PASA, 26, 139
Cristallo, S., Piersanti, L., Straniero, O., et al. 2011, ApJS, 197, 17
Cristallo, S., Straniero, O., Piersanti, L., & Gobrecht, D. 2015, ApJS, 219, 40
Cseh, B., Lugaro, M., D'Orazi, V., et al. 2018, A&A, 620, A146
Cseh, B., Világos, B., Roriz, M. P., et al. 2022, A&A, 660, A128
Cutri, R. M., Skrutskie, M. F., van Dyk, S., et al. 2003, yCat, II/246
de Castro, D. B., Pereira, C. B., Roig, F., et al. 2016, MNRAS, 459, 4299
Den Hartog, E. A., Lawler, J. E., Sobeck, J. S., Sneden, C., & Cowan, J. J. 2011, ApJS, 194, 35
Denissenkov, P. A., Herwig, F., Woodward, P., et al. 2019, MNRAS, 488, 4258
Doherty, C. L., Gil-Pons, P., Siess, L., Lattanzio, J. C., & Lau, H. H. B. 2015, MNRAS, 446, 2599
Edvardsson, B., Andersen, J., Gustafsson, B., et al. 1993, A&A, 275, 101
Escorza, A., Boffin, H. M. J., Jorissen, A., et al. 2017, A&A, 608, A100
Frebel, A. 2018, ARNPS, 68, 237
Gaia Collaboration, Katz, D., Antoja, T., et al. 2018, A&A, 616, A11
Goswami, A. 2005, MNRAS, 359, 531
Goswami, A., Aoki, W., Beers, T. C., et al. 2006, MNRAS, 372, 343
Goswami, A., Aoki, W., & Karinkuzhi, D. 2015, MNRAS, 455, 402
Goswami, P. P., & Goswami, A. 2020, JAA, 41, 47
Goswami, P. P., & Goswami, A. 2022, A&A, 657, A50
Goswami, P. P., Rathour, R. S., & Goswami, A. 2021, A&A, 649, A49
Hampel, M., Karakas, A. I., Stancliffe, R. J., Meyer, B. S., & Lugaro, M. 2019, ApJ, 887, 11
Hampel, M., Stancliffe, R. J., Lugaro, M., & Meyer, B. S. 2016, ApJ, 831, 171
Han, Z., Eggleton, P. P., Podsiadlowski, P., & Tout, C. A. 1995, MNRAS, 277, 1443
Hansen, C. J., Hansen, T. T., Koch, A., et al. 2019, A&A, 623, A128
Hansen, T. T., Andersen, J., Nordström, B., et al. 2016, A&A, 588 A3
Herwig, F., Pignatari, M., Woodward, P. R., et al. 2011, ApJ, 727 89
Hidalgo, S. L., Pietrinferni, A., Cassisi, S., et al. 2018, ApJ, 856, 125
Hinkle, K., Wallace, L., Valenti, J., & Harmer, D. 2000, Visible and Near Infrared Atlas of the Arcturus Spectrum 3727-9300 A (San Francisco, CA: ASP)
Husti, L., Gallino, R., Bisterzo, S., Straniero, O., & Cristallo, S. 2009, PASA, 26, 176
Ji, W., Cui, W., Liu, C., et al. 2016, ApJS, 226, 1
Jonsell, K., Barklem, P. S., Gustafsson, B., et al. 2006, A&A, 451, 651
Jorissen, A., Boffin, H. M. J., Karinkuzhi, D., et al. 2019, A&A, 626, A127
Jorissen, A., Van Eck, S., Mayor, M., & Udry, S. 1998, A&A, 332, 877
Jorissen, A., Van Eck, S., Van Winckel, H., et al. 2016, A&A, 586, A158
Karinkuzhi, D., Van Eck, S., Goriely, S., et al. 2021, A&A, 645, A61
Karinkuzhi, D., Van Eck, S., Jorissen, A., et al. 2018, A&A, 618, A32
Kennedy, C. R., Sivarani, T., Beers, T. C., et al. 2011, AJ, 141, 102
Koch, A., Reichert, M., Hansen, C. J., et al. 2019, A&A, 622, A159
Lawler, J. E., Hala, Sneden, C., et al. 2019, ApJS, 241, 21
Lawler, J. E., Wickliffe, M. E., den Hartog, E. A., & Sneden, C. 2001, ApJ, 563, 1075
Lawler, J. E., Wood, M. P., Den Hartog, E. A., et al. 2014, ApJS, 215, 20
Liu, Z.-W., Stancliffe, R. J., Abate, C., & Matrozis, E. 2017, ApJ, 846, 117
Lu, P. K. 1991, AJ, 101, 2229
Lucatello, S., Gratton, R. G., Beers, T. C., & Carretta, E. 2005, ApJ, 625, 833
Marigo, P. 2002, A&A, 387, 507
Masseron, T., Johnson, J. A., Plez, B., et al. 2010, A&A, 509, A93
Masseron, T., Plez, B., Van Eck, S., et al. 2014, A&A, 571, A47
McClure, R. D. 1983, ApJ, 268, 264
McClure, R. D. 1984, ApJL, 280, L31
McClure, R. D., & Woodsworth, A. W. 1990, ApJ, 352, 709
McDonald, I., Zijlstra, A. A., & Boyer, M. L. 2012, MNRAS, 427, 343
McWilliam, A. 1998, AJ, 115, 1640
Mennessier, M. O., Luri, X., Figueras, F., et al. 1997, A&A, 326, 722
Mishenina, T. V., Soubiran, C., Kovtyukh, V. V., & Korotin, S. A. 2004, A&A, 418, 551
Noguchi, K., Aoki, W., Kawanomoto, S., et al. 2002, PASJ, 54, 855
Pilachowski, C. A. 1977, A&A, 54, 465
Placco, V. M., Sneden, C., Roederer, I. U., et al. 2021, RNAAS, 5, 92
Preston, G. W., Sneden, C., Thompson, I. B., Shectman, S. A., & Burley, G. S. 2006, AJ, 132, 85
Purandardas, M., Goswami, A., Goswami, P. P., Shejeelammal, J., & Masseron, T. 2019, MNRAS, 486, 3266
Ram, R. S., Brooke, J. S. A., Bernath, P. F., Sneden, C., & Lucatello, S. 2014, ApJS, 211, 5
Reddy, B. E., Lambert, D. L., & Allende Prieto, C. 2006, MNRAS, 367, 1329
Roederer, I. U., Karakas, A. I., Pignatari, M., & Herwig, F. 2016, ApJ, 821, 37
Schuler, S. C., Margheim, S. J., Sivarani, T., et al. 2008, AJ, 136, 2244
Shejeelammal, J., Goswami, A., Goswami, P. P., Rathour, R. S., & Masseron, T. 2020, MNRAS, 492, 3708
Sneden, C., Lambert, D. L., & Pilachowski, C. A. 1981, ApJ, 247, 1052
Sneden, C., Lucatello, S., Ram, R. S., Brooke, J. S. A., & Bernath, P. 2014, ApJS, 214, 26
Sneden, C. A. 1973, PhD thesis, The Univ. Texas at Austin
Spite, M., Caffau, E., Bonifacio, P., et al. 2013, A&A, 552, A107
Stancliffe, R. J. 2021, MNRAS, 505, 5554
Starkenburg, E., Shetrone, M. D., McConnachie, A. W., & Venn, K. A. 2014, MNRAS, 441, 1217
Stephenson, C. B. 1989, Observatory, 3, 53
Straniero, O., Gallino, R., & Cristallo, S. 2006, NuPhA, 777, 311
Warner, B. 1965, MNRAS, 129, 263
Woosley, S. E., & Weaver, T. A. 1986, ARA&A, 24, 205
Worley, C. C., Hill, V., Sobeck, J., & Carretta, E. 2013, A&A, 553, A47
Yang, G.-C., Liang, Y.-C., Spite, M., et al. 2016, RAA, 16, 19
Yong, D., Norris, J. E., Bessell, M. S., et al. 2013, ApJ, 762, 26
Začs, L., Schmidt, M. R., & Schuster, W. J. 2000, A&A, 358, 1022